Defect studies of nanocrystalline zirconia powders and sintered ceramics

Jakub Čížek,[1,*] Oksana Melikhova,[1] Ivan Procházka,[1] Jan Kuriplach,[1] Radomír Kužel,[1] Gerhard Brauer,[2] Wolfgang Anwand,[2] Tatyana E. Konstantinova,[3] and Igor A. Danilenko[3]

[1]*Faculty of Mathematics and Physics, Charles University in Prague, V Holešovičkách 2, CZ-180 00 Praha 8, Czech Republic*

[2]*Institut für Ionenstrahlphysik und Materialforschung, Forschungszentrum Dresden-Rossendorf, Postfach 510119, D-01314 Dresden, Germany*

[3]*Galkin Donetsk Institute for Physics and Engineering, National Academy of Sciences of Ukraine, Luxemburg Street 72, 83114 Donetsk, Ukraine*

(Received 10 October 2009; revised manuscript received 10 December 2009; published 29 January 2010)

The main objective of the present paper is to communicate a study of defects behavior in zirconia-based nanomaterials—pressure-compacted yttria-stabilized zirconia (YSZ) nanopowders with different contents of Y_2O_3 and ceramics obtained by sintering the YZS nanopowders. In addition, YZS single crystals were also investigated. Positron annihilation techniques including positron lifetime and coincidence Doppler broadening with a conventional positron source and Doppler broadening experiments on a monoenergetic positron beam were involved in this study as the principal tools. These techniques were supplemented with transmission electron microscopy and x-ray diffraction observations. In order to get better support of the experimental data interpretation, the state-of-art theoretical calculations of positron parameters were performed for the perfect ZrO_2 lattice and selected defect configurations in the YSZ. Theoretical calculations have indicated that neither the oxygen vacancies nor their neutral complexes with substitutional yttrium atoms are capable of positron trapping. On the other hand, the zirconium vacancies are deep positron traps and obviously are responsible for the saturated positron trapping observed in the YSZ single crystals. In the compacted YSZ nanopowders, a majority of positrons is trapped either in the vacancylike defects situated in the negative space-charge layers along grain boundaries ($\tau_1 \approx 185$ ps) or in vacancy clusters at intersections of grain boundaries ($\tau_2 \approx 370$ ps). The intensity ratio I_2/I_1 was found to be correlated with the mean grain size d as $I_2/I_1 \sim d^{-2}$. A small fraction of positrons ($\approx 10\%$) form positronium in large pores ($\tau_3 \approx 2$ ns, $\tau_4 \approx 30$ ns). A significant grain growth during sintering of the YSZ nanopowders above 1000 °C was observed.

DOI: 10.1103/PhysRevB.81.024116 PACS number(s): 78.70.Bj, 61.46.Hk, 81.07.Wx

I. INTRODUCTION

Zirconia (zirconium dioxide, ZrO_2) exhibits many exceptional features:[1] a high melting point (2700 °C), a low thermal conductivity, a low electronic conductivity, a good oxygen-ion conductivity at elevated temperatures, a high strength, and an enhanced fracture toughness. Zirconia-based materials thus are promising for the use in a large area of industrial applications, for example, refractory materials, functional ceramics, ceramic glazes, oxygen sensors, solid oxide fuel cells, electroceramics, thermal barrier coatings, insulators, machining tools, abrasives and grinding media, etc. Indeed, zirconia belongs to the challenging topics of current solid-state physics and materials research. The favorable properties of ZrO_2-based materials become especially pronounced if these materials were fabricated of powders of nanoscopic size. Zirconia is a high-κ dielectric material, therefore, its application as an insulator in future nanoelectronic devices seems to be promising, too.

The three zirconia polymorphs are known to exist in nature or laboratory conditions.[1] Such a polymorphism, however, considerably restricts exploitation of the *pure* zirconia. This is because the pure ZrO_2, which is *monoclinic* at room temperature, transforms to the denser *tetragonal* phase at ≈ 1200 °C temperature. Such a transformation is accompanied with large volume changes and thus leads to a creation of cracks within the ZrO_2 structure. At temperatures higher than ≈ 1380 °C, the pure zirconia becomes *cubic*.

Obviously, a stabilization of high-temperature ZrO_2 phases is necessary to make a full use of advantageous zirconia features. It is well known[1] that the phase stabilization of zirconia can be achieved by an addition of a certain amount of the trivalent yttrium oxide (Y_2O_3, yttria) to form a solid solution in the ZrO_2 lattice. Such a system is termed as the yttria-stabilized zirconia (YSZ). The cubic phase of YSZ is stable at room temperature when more than ≈ 8 mol. % (≈ 14 wt. %) of the Y_2O_3 stabilizer is added to zirconia. In this case, the YSZ system is referred to as the fully stabilized zirconia. An amount of ≈ 3 mol. % (≈ 5.7 wt. %) of the Y_2O_3 (i.e., an amount insufficient to stabilize the cubic phase) brings the YSZ structure into the tetragonal phase after heating above 1000 °C. This system is only partially stabilized, since the tetragonal structure is metastable and it may thus coexist with the monoclinic phase below 1000 °C.

An embedment of Y_2O_3 into the ZrO_2 host lattice leads to a violation of stoichiometry resulting in a huge amount of native-oxygen vacancies and vacancy-solute atom complexes in the lattice. In the nanostructured YSZ materials, moreover, grain boundaries (GBs) occupy a significant fraction of material volume. GB's themselves and the defects associated to them (vacancylike misfit defects, vacancy clusters at intersections of GB's) become thus important open-volume structure elements in YSZ's, too. In addition, voids and pores may occur in the nanopowder YSZ materials and evolve during producing ceramics by sintering. Thus, various types of inherent open-volume structural elements, characterized with a size on a 1–100 nm scale, are expected to coexist in the YSZ nanomaterials. Generally, it is expected that such structures underlie macroscopic properties of materials. A detailed knowledge of the nature and behavior of open-volume de-

fects as well as their correlation with materials composition and preparation conditions is thus of a key importance for prospecting YSZ materials of macroscopic properties desired by industry.

The observation of positron annihilation by means of spectroscopic techniques (PAS=positron annihilation spectroscopy) is an important tool of investigations on nanostructured YSZ materials, since positrons are highly sensitive probes of nanometer-size open-volume defects acting as trapping centers for positrons.[2] Basic knowledge on defects is obtained from the measurements of positron lifetime (LT) spectra which reflect the local electron density at the positron annihilation site. The lifetimes measured for positrons trapped in a certain defect type are thus sensitive to the defect size, while the respective intensities (positron fractions) convey information about the defect concentration.

The measurements of Doppler broadening (DB) of annihilation radiation provide primarily data about the momentum distribution of electrons taking part in annihilation of a positron-electron pair. The one-detector γ-ray spectrometer allows for a measurement of the Doppler-broadened profile (DBP) of the annihilation peak around the 511 keV energy. The profile is usually characterized using the shape parameters S (the *sharpness* parameter—the relative area of the central part of the peak reflecting a contribution from the low-momentum electrons) and W (the *wing* parameter—the relative contribution from the high-momentum inner-shell electrons). For positrons trapped in open-volume defects, the annihilations with the core electrons of neighboring atoms are suppressed and, consequently, the S parameter is relatively enhanced. In this way, an additional knowledge on a role of positron trapping in the material studied is attained. In the coincidence mode of DB (CDB) experiments, introduced 30 years ago,[3] a two-dimensional energy spectrum in the region of annihilation peak is collected. This two-dimensional spectrum is subsequently reduced to the one-dimensional DBP. The peak-to-background ratio is improved by 3–4 orders of magnitude in CDB experiments with two HPGe detectors compared to the traditional one-detector arrangement,[4] allowing thus to disclose details of the profile in the high-momentum region. Usually, a lower limit of the high-momentum region, i.e., an electron momentum value at which annihilations with the inner-shell electrons start dominate, can be set as $\approx 10\times 10^{-3} m_0 c$. Since the high-momentum part of DBP arises from the inner-shell electrons of atoms near to the positron annihilation site unique data on the chemical surroundings of defects capable to trap positrons can be acquired by means of CDB technique. In the practice of CDB data analysis, the ratios of DBP with respect to a chosen reference material are produced in order to express the observed effects in a common scale.

In many porous media, a portion of implanted positrons may form positronium (Ps) in the singlet [para-Ps (p-Ps)] or triplet [ortho-Ps (o-Ps)] state,[5] ratio of the para-Ps to ortho-Ps yield being 1:3. The ortho-Ps pick-off annihilation is characterized with lifetimes of one to tens of ns and the ortho-Ps lifetime is a well recognized measure of the pore size. On the other hand, the self-annihilation of the short-lived para-Ps (lifetime of 0.125 ps in vacuum) leads to a remarkable narrowing of DBP.

An important complementary information on positron trapping comes from positron-diffusion lengths investigated via slow positron implantation spectroscopy (SPIS) experiments involving variable-energy positron beams.[4] Reliable *ab initio* calculations of positron response which started their development since the pioneer work[6] often bring a substantial assistance to the interpretation of observed PAS data.

Several PAS investigations of YSZ nanomaterials of different composition (including powders as well as sintered ceramics) have already been performed, see e.g., Refs. 7–10. Despite of these efforts, there still remains a lack of sufficiently complete and precise data on the binary YSZ materials which precludes unambiguous interpretation of PAS data.

To extend the current knowledge about zirconia-based nanomaterials, we have performed a PAS study focused on several binary YSZ materials of different composition and preparation conditions. As the main objective, the pressure-compacted nanopowders and ceramic materials, obtained from these nanopowders by sintering, were investigated. In order to get deeper insight into the microstructure of so complicated systems like these YSZ nanomaterials are, two kinds of YSZ single crystals were also included in this work. The high-resolution LT and CDB measurements with a conventional ^{22}Na positron source and the SPIS technique were utilized in the present work. For reference purposes, PAS measurements on relevant well-annealed metals (Zr, Y) were carried out, too. PAS experiments were supplemented by x-ray diffraction (XRD) and transmission electron microscopy (TEM) characterizations of YSZ's studied. Extended theoretical calculations of positron characteristics were also done for the defect-free ZrO_2 lattice, vacancy defects and vacancy-solute atom complexes. Preliminary results of our LT and CDB measurements as well as theoretical calculations have already been presented in recent conference proceedings.[11–15]

The subsequent text of the present paper is structured in the following way. In Sec. II, necessary experimental details are given. Section III contains results of experiments and calculations, obtained in the present work. Their discussion and interpretation is included in the section as well. The conclusions ensued from the present work are itemized in Sec. IV.

II. EXPERIMENTAL

A. Samples

Pressure-compacted YSZ nanopowders. Monoclinic pure ZrO_2 (Z0Y), tetragonal ZrO_2+3 mol. % Y_2O_3 (Z3Y), and cubic ZrO_2+8 mol. % Y_2O_3 (Z8Y) pressure-compacted nanopowders were investigated in the present work. The initial nanosize powders of all these systems were prepared by the coprecipitation technique starting from the water solutions of the stoichiometric compositions of $ZrO(NO_3)$ and $Y_2(NO_3)_3$ salts. The details of preparation procedure were described elsewhere.[16–18] Chemical purity of initial powders was examined by x-ray fluorescence analysis. The following impurity elements could be detected (their amounts were evaluated as oxide content in at. %, the standard deviations are given in parentheses in the units of the last significant digit):

TABLE I. Comparison of the measured and calculated positron lifetimes, τ, for reference specimens. Standard deviations are given in parentheses in units of the last significant digit. The data acquisition and evaluation procedure is described in Sec. II B.

Metal	Annealing (°C/h)	Purity (%)	Experiment, τ (ps)	Theory, τ (ps)	
				BN	GC
Zr	1000/3	99.8	156.9(4)	160.3	162.1
Y	850/1	99.9	205.3(5)	217.8	215.4

Al_2O_3—0.06(1), SiO_2—0.06(1), CeO_2—0.04(2), Sm_2O_3—0.06(3), CuO, Co_3O_4, Lu_2O_3, Ta_2O_5—<0.01 each. In the Z0Y powder, the Y_2O_3 impurity amounted 0.008(5) wt. %. The initial powders were calcinated under temperatures of 600–700 °C for 2 h. Then, the powders were uniaxially pressed into tablets of ≈10 mm diameter and ≈5 mm thickness. To examine possible impact of compaction pressure on microstructure of compacted nanopowders a series of specimens pressed by pressures 250, 500, and 1000 MPa was prepared for each composition studied in the present work.

Sintered YSZ ceramics. The sintering process was investigated on the ZrO_2+3 mol. % Y_2O_3 in this work. The Z3Y tablets, compacted under 500 MPa, were prepared as described above in this section and subjected to sintering at three different temperatures T_S=1000, 1200, and 1350 °C, respectively, in air for 2 h. Before measurements, each specimen was dried at 105 °C in air for 1 h. PAS measurements on the two YSZ single crystals were carried out in the present work: the tetragonal ZrO_2+3 mol. % Y_2O_3 and the commercially available cubic ZrO_2+9 mol. % Y_2O_3 (Crystec/Berlin).

Reference pure metals. Well-annealed high-purity Zr and Y metals were used as reference specimens for the determinations of Doppler-broadened profile ratios from the CDB measurements of the present work. These samples were examined by LT measurements and the results are summarized in Table I. It is found by LT that all the specimens exhibit a single LT component. To justify the nature of this component, theoretical calculations of positron lifetimes in the perfect lattice have been performed using the atomic superposition (ATSUP) method[6] and involving the electron-positron correlation within the Boroński-Nieminen (BN) approach[19] or gradient-correction (GC) scheme.[20] The measured positron lifetimes are compared in the table with the calculated ones. Since a reasonable agreement between the measured and calculated values was obtained, the reference specimens can be considered as virtually defect-free materials in which practically all positrons annihilate from the free, delocalized state.

B. PAS apparatus and data acquisition process

Positron lifetime measurements. The positron source of about 1.3 MBq was made of carrier-free $^{22}Na_2CO_3$ water solution (iThemba Laboratories) dried and sealed between ≈4 μm mylarC foils (DuPont). The LT measurements were carried out using a fast-fast BaF_2 spectrometer similar to that described in Ref. 21. The LT spectrometer exhibited a time resolution of 160 ps [full width at half maximum (FWHM) for ^{22}Na], ≈100 coincidence events per second (a peak-to-background ratio ≈10^3) for the above positron source. At least 10^7 events were accumulated in each LT spectrum. The LT spectra were decomposed into individual discrete components by means of a maximum-likelihood-based procedure.[21] The contribution of positron annihilation in the source and covering foils was measured for a well-annealed pure α iron (the bulk lifetime of 107.0±0.3 ps) and recalculated for a particular material under study according to a method suggested in Ref. 22.

Coincidence Doppler broadening measurements. The CDB measurements were carried out with a two-detector (HPGe) apparatus.[23] Using the above positron source, the CDB spectrometer exhibited an energy resolution of 1.0 keV (FWHM) at 511 keV energy and a coincidence count rate of ≈500 s^{-1} (a peak-to-background ratio of ≈10^5). Typically ≈10^8 counts were collected in each two-dimensional CDB spectrum. The spectrum was then reduced to the one-dimensional DBP cuts. The relative changes in DBP's were described in terms of the ratios of the DBP cuts to that of the pure Zr reference material. The DBP's were also characterized with ordinary shape parameters, S and W, respectively, which express the relative peak areas for the central (low-momentum) and wing (high-momentum) parts of the peak. The central region for the S parameter included electron momenta p, for which $|p|<2.7\times10^{-3}m_0c$, while the region of $|p|>7.4\times10^{-3}m_0c$ was used for the determination of the W parameter.

Slow-positron implantation spectroscopy. The SPIS measurements were performed using a magnetically guided monoenergetic positron beam—the SPONSOR facility.[24] Positron energies were selected so that they covered the region from 30 to 35 keV. The diameter of the beam spot was ≈4 mm for all positron energies. Energy spectra of annihilation γ rays were measured with a HPGe detector having an efficiency of ≈30% and energy resolution (FWHM) of (1.06±0.01) keV at 511 keV. The dependencies of S and W parameters on the positron energy were measured and then analyzed by means of the VEPFIT code.[25]

III. RESULTS AND DISCUSSION

A. Theoretical calculations

We first give a short overview of the current understanding of vacancylike defects and their clusters in YSZ. Y ions

substitute Zr ones, which results in the formation of oxygen vacancies that compensate electrostatically the YSZ lattice. Specifically, Zr ions or Zr^{4+} denoted further as $Zr^{\bullet\bullet\bullet\bullet}$ (the so-called Kröger-Vink notation[26] is used throughout this paper) have a different charge than substituting Y^{3+} ions (Y'_{Zr}) having thus −1 charge relative to the lattice. As oxygen vacancies, $V_O^{\bullet\bullet}$, have a charge of +2, there are two Y'_{Zr} ions per one $V_O^{\bullet\bullet}$ to keep the YSZ lattice neutral. Extended x-ray absorption fine-structure studies[27,28] have suggested that Y'_{Zr} preferentially occupies a site which is the next-nearest-neighbor (NNN) to the oxygen vacancy instead of the nearest-neighbor (NN) sites that were originally expected to be places for Y'_{Zr} because of attractive electrostatic attraction of $V_O^{\bullet\bullet}$ and Y'_{Zr}. This finding is in agreement with recent *ab initio* calculations[29] that have shown that a $V_O^{\bullet\bullet}Y'_{Zr}$ complex has the lowest energy when yttrium is located in the NNN site. It has also been shown that at low temperatures only a relatively small fraction of oxygen vacancies is unassociated with Y'_{Zr}. At low yttrium concentrations the majority of oxygen vacancies couples with a single substitutional yttrium atom forming an $V_O^{\bullet\bullet}Y'_{Zr}$ complex,[30,31] while at a higher yttrium content the complexes with two yttrium atoms ($Y'_{Zr}V_O^{\bullet\bullet}Y'_{Zr}$) dominate.

Neutron-diffraction experiments[32,33] further confirm the conclusion regarding the atomistic structure of the $Y'_{Zr}V_O^{\bullet\bullet}Y'_{Zr}$ complex (see also Ref. 34 for electron-diffraction data). Goff *et al.*[32] also showed that oxygen vacancies have a tendency to be aligned in the ⟨111⟩ directions creating thus oxygen divacancies with one Zr ion separating them.

In order to have an idea whether the above $V_O^{\bullet\bullet}$-related defects may trap positrons and what are their corresponding positron characteristics, selected point defects, their complexes, and further more complicated defect structures were examined in the present work. In particular, the oxygen vacancy ($V_O^{\bullet\bullet}$) and two oxygen-vacancy complexes with substitutional yttrium atoms, viz. $Y'_{Zr}V_O^{\bullet\bullet}Y'_{Zr}$ and $2Y'_{Zr}V_O^{\bullet\bullet}Zr_{Zr}^{\times}V_O^{\bullet\bullet}2Y'_{Zr}$, were studied. In addition, we also consider the zirconium vacancy (V_{Zr}'''') that may be present in YSZ materials for various reasons, like a slight Zr nonstoichiometry[35] or high-valence impurities,[8,36] though the V_{Zr}'''' formation energy is quite high (see Ref. 37 for the data on the monoclinic phase). As a reference we also studied the defect-free ZrO_2 lattice. The present positron calculations included the positron lifetime τ, the high-momentum part (HMP) of the momentum distribution of annihilation photons, as well as the positron binding energy E_b to defects, the last being defined as

$$E_b = E_f - E_d, \tag{1}$$

where E_f is the ground-state energy of a free, delocalized positron in the perfect ZrO_2 lattice and E_d is the ground-state energy of a positron trapped at a particular defect.

We further refer to the review by Puska and Nieminen[38] regarding the theoretical background of positron calculations. Except for an early work[39] we are not aware of any computational positron study of ZrO_2 and related materials.

TABLE II. Calculated positron lifetimes τ and positron binding energies E_b for various positron states in cubic and tetragonal ZrO_2 rigid lattices.

	ATSUP-BN		ATSUP-GC	
	τ (ps)	E_b (eV)	τ (ps)	E_b (eV)
	Cubic phase			
Perfect lattice	138		146	
$V_O^{\bullet\bullet}$	140	0.02	149	0.03
$Y'_{Zr}V_O^{\bullet\bullet}Y'_{Zr}$	138	<0.01	147	<0.01
$2Y'_{Zr}V_O^{\bullet\bullet}Zr_{Zr}^{\times}V_O^{\bullet\bullet}2Y'_{Zr}$	144	0.02	153	0.06
V_{Zr}''''	196	2.72	222	2.44
$V_O^{\bullet\bullet}$ superstructure	153		159	
	Tetragonal phase			
Perfect lattice	141		150	
$V_O^{\bullet\bullet}$	142	0.02	152	0.03
$Y'_{Zr}V_O^{\bullet\bullet}Y'_{Zr}$	141	<0.01	150	<0.01
V_{Zr}''''	198	2.56	224	2.28
$V_O^{\bullet\bullet}$ superstructure	156		163	

1. Nonrelaxed defects

Calculations of τ and E_b were at first performed for the case of a *rigid* lattice, when atomic relaxations around defects were neglected. The effective potential for positrons was constructed using atomic densities of free atoms within the ATSUP method[6,40] already mentioned above. Electron-positron correlations were taken into account in two ways: (i) within the BN approach[19] taking into account incomplete positron screening[41] considering a dielectric constant of $\varepsilon_\infty = 4.62$ and (ii) within the GC scheme.[20] The charge state of defects is not considered in the present calculations, i.e., studied defects are taken to be neutral. Supercells considered in positron calculations are mostly based on the $4\times4\times4$ multiplication of the cubic fluorite cell of ZrO_2 in three dimensions, i.e., totally 768 atoms (256 Zr and 512 O). In some cases smaller supercells were used, as indicated below.

The positron lifetimes and binding energies calculated in the present work for the cubic and tetragonal ZrO_2 phases are collected in Table II. It is seen from the table that differences in positron parameters for both these phases are very small, regardless of using either of approaches BN or GC. For example, positron lifetimes differ by a few picosecond ($<3\%$). Such a behavior is not surprising, because the volume per formula unit in the tetragonal phase amounts to 33.07 Å^3 while in the cubic phase it is 32.97 Å^3 (Ref. 42). The tetragonal phase exhibits slightly prolonged positron lifetimes compared to the cubic phase due to its more open structure. Results in Table II show that $V_O^{\bullet\bullet}$ represents a too shallow potential well for positrons and is thus incapable of positron trapping. The same conclusion can be drawn for $Y'_{Zr}V_O^{\bullet\bullet}Y'_{Zr}$ complexes. We note that the $Y'_{Zr}V_O^{\bullet\bullet}Y'_{Zr}$ complex with compensated electric charge was suggested as a dominant positron trapping site in YSZ crystals in Refs. 9 and 43. On the

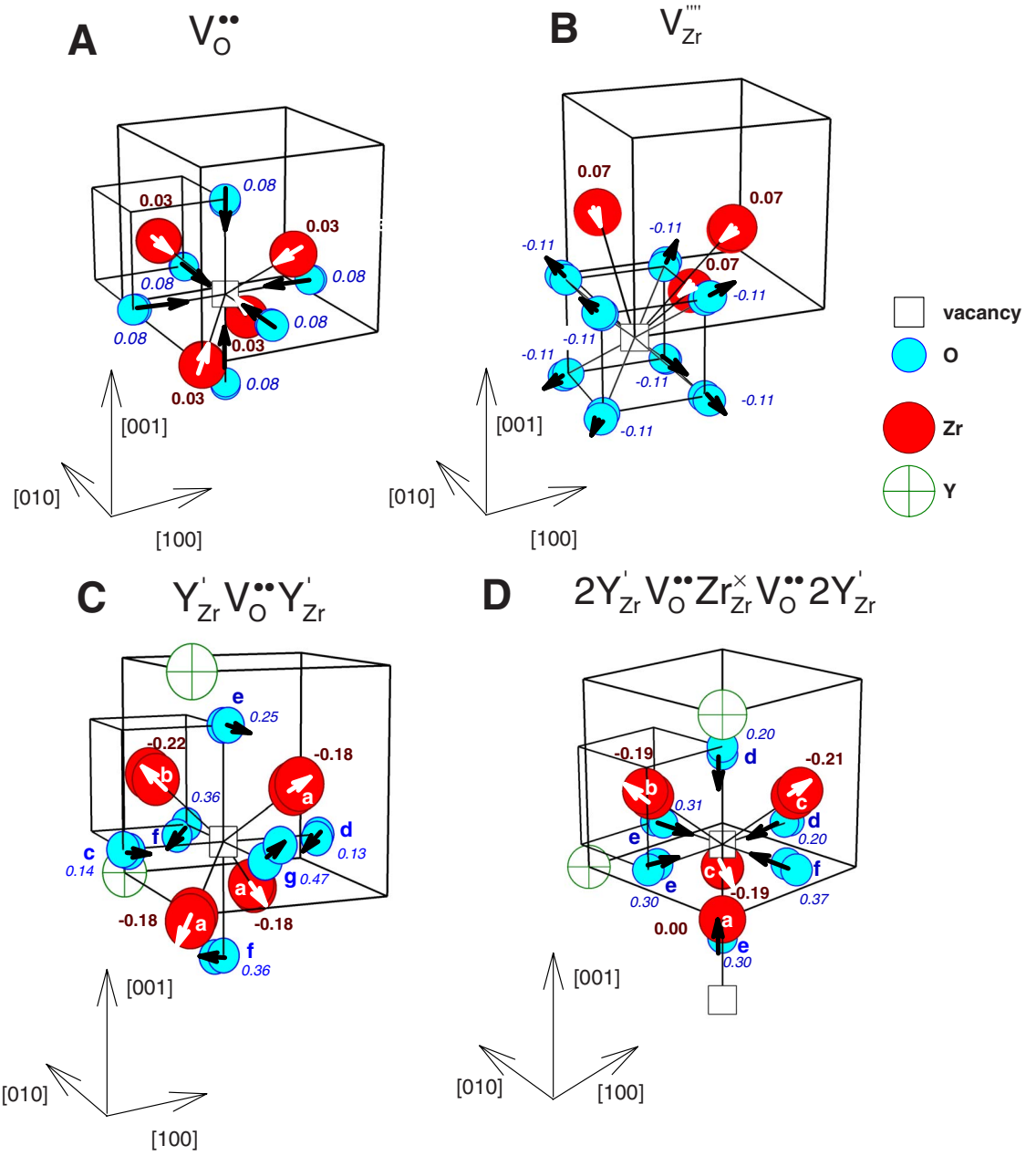

FIG. 1. (Color online) Relaxed defect geometries for various defects calculated using the GGA pseudopotential. The values given are atom displacements in angstrom. A positive value of displacement means an inward relaxation, while a negative sign of displacement stands for an outward relaxation. The letters denote atoms undergoing similar relaxation, cf. Table III.

other hand, V''''_{Zr} is a deep potential well capable to confine the positron wave function.

The concentration of oxygen vacancies is rather high due to a violation of stoichiometry caused by an addition of the Y_2O_3 stabilizer and as we mentioned above there is an interaction between closely spaced oxygen vacancies, which results in an ordering of these defects. As a first guess, one may consider a superstructure of ordered oxygen vacancies rather than an isolated $V_O^{\bullet\bullet}$. Although an isolated oxygen vacancy is unable to confine a positron, an array of such vacancies increases open volume in the lattice and could thus prolong the lifetime of free positrons. In our calculations, therefore, a superstructure of oxygen vacancies was also considered. It was modeled by removing one oxygen atom from a twelve-atom cell of ZrO_2 applying periodic boundary conditions. Certainly, one can see in Table II that our calculations for such a $V_O^{\bullet\bullet}$ superstructure yielded a higher positron lifetime compared to an isolated $V_O^{\bullet\bullet}$ and also to the perfect ZrO_2 lattice.

Furthermore, the $2Y'_{Zr}V_O^{\bullet\bullet}Zr_{Zr}^{\times}V_O^{\bullet\bullet}2Y'_{Zr}$ complex is a symmetrical configuration of two $Y'_{Zr}V_O^{\bullet\bullet}Y'_{Zr}$ complexes with their $V_O^{\bullet\bullet}$'s aligned along a ⟨111⟩ direction and separated by a Zr atom [see Fig. 1(D)] as suggested from neutron-diffraction experiments.[32] The positron lifetime and binding energy results indicate, as for the $Y'_{Zr}V_O^{\bullet\bullet}Y'_{Zr}$ case, that this defect/complex does not constitute a positron trap.

TABLE III. Calculated displacements, d, and projected displacements, d_p, of atoms due to lattice relaxations around various defects (see the text for further explanations). The superscripts used within the Table refer to ion's designation in Figs. 1(A)–1(D).

	NN			NNN			
Defect	Atom	Direction	d (Å)	Atom	Direction	d (Å)	d_p (Å)
$V_O^{\bullet\bullet}$	Zr	⟨111⟩	+0.03	O	⟨100⟩	+0.08	
$Y'_{Zr}V_O^{\bullet\bullet}Y'_{Zr}$	Zr	⟨111⟩	−0.18[a]	O	$\langle 3\bar{1}\bar{1}\rangle$	0.14	+0.13[c]
		⟨111⟩	−0.22[b]		$\langle\bar{1}\bar{1}\bar{1}\rangle$	0.13	+0.08[d]
					$\langle 0\bar{1}0\rangle$	0.25	−0.03[c]
					⟨101⟩	0.36	−0.10[f]
					$\langle\bar{1}3\bar{1}\rangle$	0.47	−0.10[g]
$2Y'_{Zr}V_O^{\bullet\bullet}Zr_{Zr}^{\times}V_O^{\bullet\bullet}2Y'_{Zr}$	Zr		0.0[a]	O	⟨100⟩	+0.20[d]	
		⟨111⟩	−0.19[b]		⟨100⟩	+0.30[e]	
		⟨111⟩	−0.21[c]		⟨100⟩	+0.37[f]	
V_{Zr}''''	O	⟨111⟩	−0.11	Zr	⟨110⟩	+0.07	

2. Relaxed defects

Lattice relaxations around defects in oxides (including ZrO_2) are known to be rather large.[29,44] Hence, the consideration of a rigid lattice in theoretical calculations may be an oversimplification. To improve *ab initio* modeling of defects in ZrO_2 and to examine the role of atomic relaxations in it, we employed the Vienna *ab initio* simulation package (the VASP code[45–48]) to find out relaxed geometries of studied defects. For this purpose, we have minimized the total energy of supercells containing studied defects with respect to atomic/ionic positions. Because of above mentioned very small differences in positron parameters for the tetragonal and cubic rigid lattices, calculations involving ion relaxations were performed for the cubic lattice only. As the cubic ZrO_2 (fluorite) lattice with a small yttrium content is not, in general, stable with respect to small deviations of oxygen atoms from their ideal positions and tends to transform to the tetragonal lattice,[49] we have attempted to restrict the symmetry considered in relaxations to the cubic one to avoid such a transformation whenever it is possible to do so.

4*s*, 4*p*, 5*s*, and 4*d* Zr and Y electrons and 2*s* and 2*p* O electrons were included in the *ab initio* VASP pseudopotential calculations of electronic structure and ion relaxations. In the course of calculations, projector augmented-wave pseudopotentials (PPs) within the local-density and generalized gradient approximations (GGA) were employed.[50] As the results obtained with both PPs are very similar, only those calculated within GGA approach are shown and discussed in the following text. We also mention that the GGA approach is often preferred in first-principles studies of ZrO_2 and YSZ.[51] In the course of calculations, we used 96 atom supercells ($2\times2\times2$ multiplication of the cubic fluorite cell) employing $2\times2\times2$ **k**-mesh sampling.

We first treated intrinsic vacancies $V_O^{\bullet\bullet}$ and V_{Zr}'''' and two $V_O^{\bullet\bullet}$ complexes containing yttrium atoms, i.e., $Y'_{Zr}V_O^{\bullet\bullet}Y'_{Zr}$ and $2Y'_{Zr}V_O^{\bullet\bullet}Zr_{Zr}^{\times}V_O^{\bullet\bullet}2Y'_{Zr}$. The calculated relaxations are shown schematically in Figs. 1(A)–1(D) and the displacements of NN and NNN ions are summarized in Table III. The superscripts used within the table refer to ions' designations in Figs. 1(A)–1(D). Ions exhibiting similar relaxation are denoted by the same letter. Calculated displacements d of atoms in the NN and NNN sites around defects are listed in the table together with the direction of the ion's relaxation. In the case that an ion relaxes in a direction, which differs from the vector connecting the defect and the ion in question, the table shows also the projection of the displacement, d_p, onto the connecting line between the defect and the ion in the rigid lattice. The plus sign marks an inward relaxation, while the minus sign denotes an outward relaxation.

In the case of $V_O^{\bullet\bullet}$, the largest relaxation can be seen for oxygen NNN atoms which move toward the vacancy along ⟨100⟩ directions. Such a relaxation can be expected from the attractive Coulomb interaction between the +2-charged oxygen vacancy and oxygen anions. The NN zirconium atoms exhibit a smaller relaxation along ⟨111⟩ directions, which is also inward, i.e., toward the vacancy. We note that in Ref. 29 apparently larger relaxations were obtained for the vacancies NN's and NNN's using the same supercell (i.e., ZrO_2 +3 mol. % Y_2O_3) compared to the present work. This is due to forcing the $V_O^{\bullet\bullet}$ symmetry to be cubic in different ways (see Ref. 29 for details).

One can see in Figs. 1(A) and 1(D) that the displacement pattern for $2Y'_{Zr}V_O^{\bullet\bullet}Zr_{Zr}^{\times}V_O^{\bullet\bullet}2Y'_{Zr}$ looks very similar to that of $V_O^{\bullet\bullet}$. Thus, the presence of two yttrium atoms in the NNN sites modify only slightly the relaxed geometry of $V_O^{\bullet\bullet}$. The main effect of yttrium dopants is an increased relaxation of the adjacent oxygen atom along the ⟨100⟩ direction due to a superposition of $V_O^{\bullet\bullet}$ attraction and Y'_{Zr} repulsion. A symmetrical configuration of two $V_O^{\bullet\bullet}$'s around the central Zr atom causes that the forces acting on this central atom due to these NN vacancies cancel each other and the central Zr atom thus remains in its rigid lattice position.

Contrary to $2Y'_{Zr}V_O^{\bullet\bullet}Zr_{Zr}^{\times}V_O^{\bullet\bullet}2Y'_{Zr}$, the $Y'_{Zr}V_O^{\bullet\bullet}Y'_{Zr}$ complex was found to destabilize the cubic structure that was not possible to keep, contrary to other investigated defects. In-

TABLE IV. Calculated positron lifetimes, τ, and positron binding energies, E_b, for relaxed defect geometries. The effective positron potential was modeled by atomic superposition, i.e., neglecting the charge-transfer effects. The BN and GC approaches for electron-positron correlation were applied in the calculations (see text).

	BN		GC	
Positron state	τ (ps)	E_b (eV)	τ (ps)	E_b (eV)
Perfect lattice	138		146	
$V_O^{\bullet\bullet}$	139	0.01	147	0.02
$Y'_{Zr}V_O^{\bullet\bullet}Y'_{Zr}$	164	0.30	173	0.38
$2Y'_{Zr}V_O^{\bullet\bullet}Zr_{Zr}^{\times}V_O^{\bullet\bullet}2Y'_{Zr}$	156	0.20	165	0.26
V_{Zr}''''	216	2.75	238	2.60

TABLE V. Calculated positron lifetimes, τ, and positron binding energies, E_b, for relaxed defect geometries. Positron parameters were calculated using the self-consistent electron density obtained by VASP, i.e., the charge-transfer effects were involved in this approach. The BN approximation for electron-positron correlations was applied in the calculations.

	BN	
Positron state	τ (ps)	E_b (eV)
Perfect lattice	133	
$V_O^{\bullet\bullet}$	132	−0.12
$Y'_{Zr}V_O^{\bullet\bullet}Y'_{Zr}$	139	0.04
$2Y'_{Zr}V_O^{\bullet\bullet}Zr_{Zr}^{\times}V_O^{\bullet\bullet}2Y'_{Zr}$	134	0.01
V_{Zr}''''	220	2.80

deed, one can see in Fig. 1(C) that the relaxed geometry of $Y'_{Zr}V_O^{\bullet\bullet}Y'_{Zr}$ involves rather complicated relaxations of NN oxygen atoms in directions, which do not coincide with the radius vector from the vacancy toward the corresponding atom. A closer inspection of these relaxations reveals that NNN oxygen atoms tend to create a configuration typical for the tetragonal phase. This is slightly modified by the two substitutional Y atoms in adjacent sites which cause that the relaxation of O atoms depends also on their distance from the Y dopants. However, the general trend seen clearly in the $Y'_{Zr}V_O^{\bullet\bullet}Y'_{Zr}$ complex relaxed geometry is a disruption of the cubic structure.

In the case of V_{Zr}'''', the NN oxygen cations exhibit an outward relaxation along ⟨111⟩ directions, as expected due to the −4 charge of a zirconium vacancy. On the other hand, the NNN zirconium atoms move toward the vacancy along ⟨110⟩ directions.

Two approaches were employed for the calculation of positron parameters for the relaxed defects.

(i) Relaxed defect configurations were treated within the conventional ATSUP scheme, i.e., the effective positron potential was constructed from a superposition of electron densities and Coulomb potentials of free atoms located at relaxed positions. Hence, the charge transfer among atoms and consequently the ionic character of the studied material are neglected in this approach.

(ii) The one-particle Schrödinger equation was solved for a positron in an effective potential obtained from the self-consistent electron density and Coulomb potential determined for the relaxed defect geometry by VASP. Thus, in this approach the charge transfer is involved.

For the purpose of positron calculations, the relaxed VASP supercells were extended to a total of 768 atoms by adding atoms at sides of VASP supercells. Such added atoms are arranged in the form of the regular ZrO_2 lattice. The positron lifetimes and positron binding energies to defects, calculated within the approaches (i) and (ii), respectively, are collected in Tables IV and V. We shall first present the results of the (i) approach.

Considering relaxations discussed above it can be deduced that the open volume of $V_O^{\bullet\bullet}$ was *reduced* in the relaxed configuration because both NN (zirconium) and NNN (oxygen) atoms relaxed toward the defect. Thus it can be concluded that $V_O^{\bullet\bullet}$, which was found to be unable of positron trapping in the rigid lattice geometry, is in its relaxed configuration even less attractive for positrons. Indeed, one can see in Table IV that the positron lifetime in a supercell containing $V_O^{\bullet\bullet}$ is almost equal to the bulk lifetime and the positron binding energy to a relaxed oxygen vacancy is negligible. On the other hand, the open volume of V_{Zr}'''' becomes *larger* in the relaxed configuration due to a relatively large outward relaxation of NN oxygen cations. Hence the relaxed V_{Zr}'''' is a deeper positron trap and the lifetime of trapped positrons becomes larger than that for a V_{Zr}'''' in the rigid lattice.

When the charge transfer is taken into account [approach (ii)], the ionicity of the ZnO crystal structure becomes apparent and is manifested through the positron attraction to oxygen anions, which leads to a higher annihilation rate with oxygen electrons and, thereby, to an overall decrease in the positron lifetime, which was indeed observed in the case of the perfect lattice, $V_O^{\bullet\bullet}$ and complexes consisting of $V_O^{\bullet\bullet}$ coupled with Y. One can see in Table V that a positively charged $V_O^{\bullet\bullet}$ repels a positron and forces it to lattice regions with a higher electron density causing thus a shortening of the positron lifetime as well as an increase in the positron energy. A similar effect was found also in the case of the $Y'_{Zr}V_O^{\bullet\bullet}Y'_{Zr}$ and the $2Y'_{Zr}V_O^{\bullet\bullet}Zr_{Zr}^{\times}V_O^{\bullet\bullet}2Y'_{Zr}$ complex. The open volume of these complexes was extended due to outward relaxations of NN Zr atoms [see Fig. 1(C)]. This is reflected by a raise of the positron lifetime and binding energy calculated for the relaxed $Y'_{Zr}V_O^{\bullet\bullet}Y'_{Zr}$ and $2Y'_{Zr}V_O^{\bullet\bullet}Zr_{Zr}^{\times}V_O^{\bullet\bullet}2Y'_{Zr}$ geometries in Table IV. However, Table V shows that if the charge transfer is taken into account, then the complexes are not capable of positron trapping anymore due to the Coulombic repulsion of the positron and oxygen vacancy. Binding energies of positrons to $Y'_{Zr}V_O^{\bullet\bullet}Y'_{Zr}$ and $2Y'_{Zr}V_O^{\bullet\bullet}Zr_{Zr}^{\times}V_O^{\bullet\bullet}2Y'_{Zr}$ defects, as given in Table V, are very small and would vanish with the increasing supercell size used for positron calculations.

Contrary to other defects, a slight increase in the positron lifetime was observed for V_{Zr}'''' when the charge transfer was taken into account. Also in this case positrons are attracted to

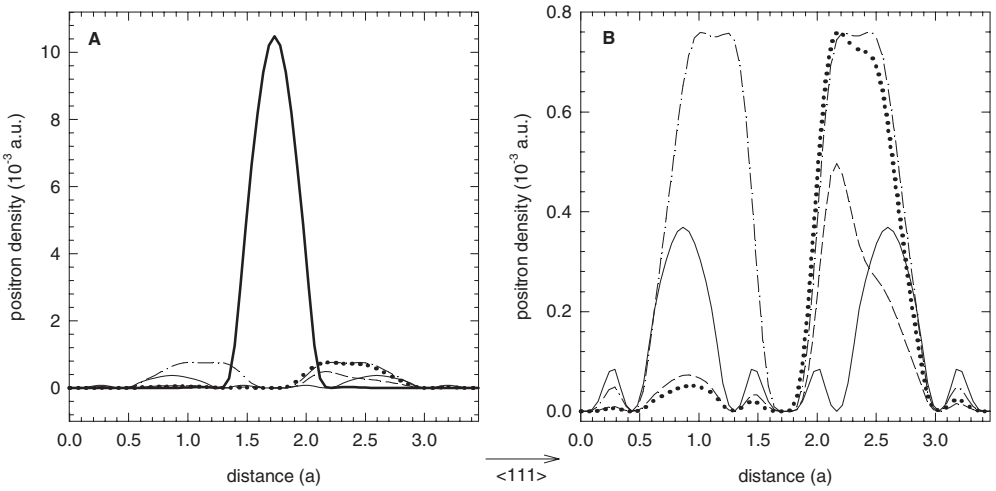

FIG. 2. (a) Positron density $|\psi_+|^2$ along the ⟨111⟩ direction calculated for a perfect ZrO_2 crystal (solid line) and a crystal containing various defects: $V_O^{\bullet\bullet}$ (dashed line), $Y'_{Zr}V_O^{\bullet\bullet}Y'_{Zr}$ (dotted line), $2Y'_{Zr}V_O^{\bullet\bullet}Zr_{Zr}^{\times}V_O^{\bullet\bullet}2Y'_{Zr}$ (dash-dotted line), and V_{Zr}'''' (thick solid line). (b) A zoom of the positron density around defects which are not capable of positron trapping. Positron densities were calculated with charge transfer taken in the approach (ii) in the text. The oxygen (or zirconium) vacancy was always situated in the 1 1 1 position. Positron density is expressed in atomic units and the distance scale is in the units of ZrO_2 lattice constant a.

negatively charged oxygen ions, but because of a more complicated nature of charge redistribution due to self-consistency leading to a lower electron density inside the vacancy, the resulting positron lifetime is finally moderately prolonged.

Positron densities $|\psi_+|^2$ calculated using the approach (ii) for free positrons in the perfect ZrO_2 lattice and for the defect configurations considered in Table III are plotted in Figs. 2(A) and 2(B) in the ⟨111⟩ direction. One can see in Fig. 2(A) that a positron is confined in V_{Zr}''''. On the other hand, the defects connected with an oxygen vacancy cause only a slight local enhancement in the amplitude of the positron density, but do not form a bound positron state. Contrary to the case of V_{Zr}'''', the positron density is diminished in a $V_O^{\bullet\bullet}$ center due to its positive charge. Local maxima of the positron density can be seen around an oxygen vacancy in the "open volume" between vacancy and NN ions. As one can see in Fig. 2(B), the magnitude of the positron density in the vicinity of $V_O^{\bullet\bullet}$ is similar to that in a perfect lattice. A higher amplitude of the positron density around an oxygen vacancy can be seen in $V_O^{\bullet\bullet}$ associated with yttrium atoms. This is a consequence of an enlargement of the open volume caused by ion displacements induced by yttrium atoms in the NNN sites. However, the open volume around an oxygen vacancy is still too small to form a localized positron state.

It should be mentioned that atomic relaxations in this work were performed without a positron trapped inside the defects examined. However, in a real defect, the trapped positron acts on the surrounding atoms by the so-called positron-induced forces[52] that can be evaluated using the Hellman-Feynman theorem.[53] Thus, the relaxed geometry of a defect *with* a trapped positron may differ from that calculated *without* a positron. Recent calculations[54] for monovacancies in Si, Al, and Cu showed that the effect of positron-induced forces on atomic relaxations may be significant. Thus, it would be useful to include positron-induced forces into theoretical positron calculations for various defects in YSZ. Such a refined approach could somewhat modify the picture given here, especially regarding the question of positron trapping in $Y'_{Zr}V_O^{\bullet\bullet}Y'_{Zr}$ complexes. However, it cannot be expected that $V_O^{\bullet\bullet}$ will be able to trap positrons even if positron-induced forces are taken into account (see also Ref. 44). Regarding V_{Zr}'''', the trapped positron is expected to attract NN oxygen ions. An inward relaxation of these ions would shorten the lifetime of trapped positrons. However, details remain to be determined finally in a future work.

In the VASP calculations oxygen vacancy was created by removing a neutral O atom, hence, it has +2 charge relative to the lattice. Other charge states of oxygen vacancy can be stabilized, depending on the stoichiometry of YSZ and the Fermi level position in the band gap. In analogy with other oxides, $V_O^{\bullet\bullet}$ may capture electron and form F^+ center.[55,56] It was found[29] that single occupied F^+ centers are only marginally stable and decay into neutral, doubly occupied F centers, and $V_O^{\bullet\bullet}$. However, ATSUP calculations for rigid lattice performed in Sec. III A 1 demonstrated that simply due to geometrical reasons oxygen vacancy likely does not constitute positron trap even as single occupied F^+ center or doubly occupied neutral F center. However, refined calculations of oxygen vacancies in various charge states are desirable to obtain defined conclusion about this problem.

To summarize, from theoretical calculations just discussed it can be concluded that $V_O^{\bullet\bullet}$ and most probably also $Y'_{Zr}V_O^{\bullet\bullet}Y'_{Zr}$ and $2Y'_{Zr}V_O^{\bullet\bullet}Zr_{Zr}^{\times}V_O^{\bullet\bullet}2Y'_{Zr}$ complexes should be excluded from a set of possible positron trapping sites in YSZ. On the other hand, V_{Zr}'''' is undoubtedly a deep positron trap. Positron lifetime may be prolonged by the existence of correlated clusters or chains of $V_O^{\bullet\bullet}$, as proposed, e.g., in Refs. 34 and 57.

3. High-momentum parts of momentum distribution

The HMP calculations were performed using ATSUP-based approach described in Refs. 58 and 59. This approach enables to calculate contribution of core electrons, which are

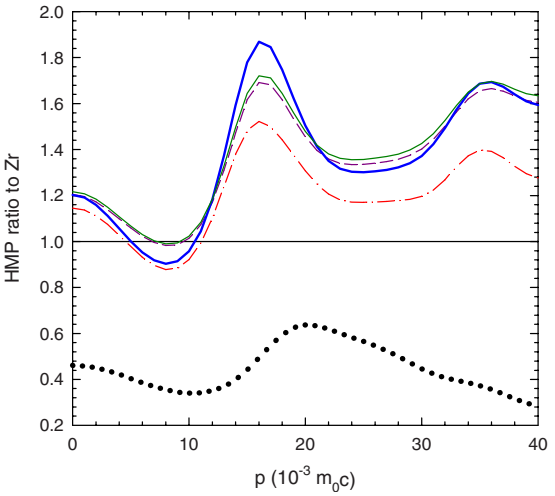

FIG. 3. (Color online) Calculated HMP ratios (related to the defect-free Zr) for various positron states in ZrO_2: perfect ZrO_2 (thin solid line), $V_O^{\bullet\bullet}$ (dashed line), V_{Zr}'''' (thick solid line), and $Y'_{Zr}V_O^{\bullet\bullet}Y'_{Zr}$ (dash-dotted line). For comparison, HMP ratio for pure Y was also calculated (dotted line). The curves were calculated for relaxed defect configurations (GGA pseudopotential) and using the GC approach for the positron-electron correlation.

almost unaffected by crystal bonding and can be well described by atomic orbitals, to the momentum distribution of annihilation radiation. On the other hand, ATSUP-based approach cannot describe accurately contribution of valence electrons. For this reason only core electrons were included in the calculations of momentum distributions and comparison of calculated HMP curves with experiment is, therefore, meaningful only in the high-momentum region, where annihilations with core electrons dominate. Core electron configurations employed in HMP calculations were as follows. In the case of Zr (Y), electrons with a configuration of a Kr atom plus two (one) $4d$ ones were considered to act as core electrons. It has to be noted that $4d$ electrons have actually a "semicore" character, therefore, their attribution to core electrons is not obvious. To select "best" core electron configurations we performed HMP calculations for pure Zr or Y and compared the calculated momentum distributions with experimental CDB profiles measured on pure Zr or Y reference samples. It was found that configurations with $4d$ orbitals treated as core electrons exhibit better agreement with experiment and describe well the experimental CDB curves in the high-momentum range ($p > 10 \times 10^{-3} m_0 c$). For O, the $1s^2$, $2s^2$, and $2p^2$ orbitals were considered as core electrons.

The calculated HMP ratio curves for $V_O^{\bullet\bullet}$, $Y'_{Zr}V_O^{\bullet\bullet}Y'_{Zr}$, and V_{Zr}'''' related to defect-free Zr are plotted in Fig. 3. All HMP ratios exhibit a pronounced peak at $p \approx 15 \times 10^{-3} m_0 c$, which comes from positrons annihilated by $2p$ oxygen electrons. The amplitude of this peak can serve for prediction of a fraction of positrons annihilated by oxygen electrons. In the calculations it was found that ≈70% of positrons trapped in V_{Zr}'''' annihilate with oxygen electrons. Delocalized positrons in perfect ZrO_2 are annihilated by oxygen electrons approximately in 50% cases, see the corresponding curve in Fig. 3. In the case of ZrO_2 containing $V_O^{\bullet\bullet}$, the fraction of positrons annihilated by oxygen electrons is further reduced slightly

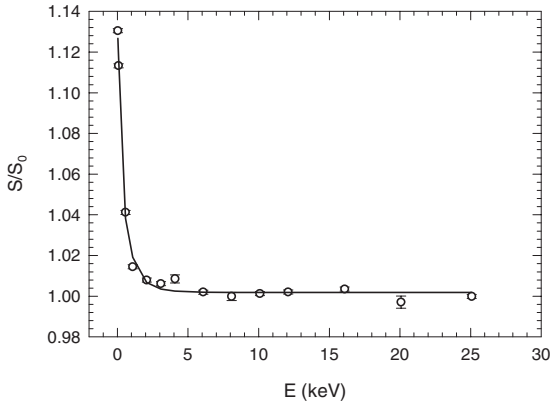

FIG. 4. Dependence of the S parameter (open circles) on the positron energy the E for ZrO_2+9 mol. % Y_2O_3 single crystal. The S parameter was normalized to the bulk value S_0 measured at E =25 keV. The solid line shows a model curve fitted by the VEPFIT package (Ref. 25) within the single-layer model.

below 50%. The HMP curve for $Y'_{Zr}V_O^{\bullet\bullet}Y'_{Zr}$ with an oxygen vacancy associated with yttrium atoms is shifted below the curve for $V_O^{\bullet\bullet}$ due to positron trapping occurring for this defect when the scheme (i) is used for positron calculations [HMP calculations within scheme (ii) are not available]. A closer inspection shows that a contribution of positron annihilations with yttrium electrons is very small and can hardly be detected in experiment.

B. ZrO_2+9 mol. % Y_2O_3 single crystal

The LT, SPIS, and CDB measurements were performed on the ZrO_2+9 mol. % Y_2O_3 single crystal in the present work. The measured LT spectrum exhibited a single component with a lifetime of (175 ± 1) ps. This lifetime is substantially longer than the lifetime of ≈133 ps calculated for delocalized positrons, see Sec. III A, which strongly suggests that positron trapping plays a dominant role. On the other hand, the measured lifetime is considerably shorter than the theoretical lifetime of positrons trapped in V_{Zr}'''', which was shown in Sec. III A to be the only defect capable of positron trapping. Thus, the interpretation of the lifetime component observed in the ZrO_2+9 mol. % Y_2O_3 single crystal is not straightforward.

To gain further information about the positron behavior in the ZrO_2+9 mol. % Y_2O_3 single crystal, we have studied the positron diffusion back to the surface using the SPIS technique. In Fig. 4, the measured dependence of the S parameter on the positron energy is shown together with a curve fitted by the VEPFIT software[25] assuming a simple single-layer model. A very short positron diffusion length, $L_+ = (8.6 \pm 0.4)$ nm, was obtained from fitting. This result, similar to that obtained for a ZrO_2 cubic single crystal by Grynszpan *et al.*,[60] gives a clear evidence that virtually all positrons in the ZrO_2+9 mol. % Y_2O_3 single crystal annihilate from a trapped state at defects. Consequently, the observed LT component with the lifetime of 175 ps must be attributed to a single type of defects (saturated defect trapping). An order of magnitude of the defect concentration, C, can be estimated using the relation

$$C = \frac{1}{\nu\tau_B}\left(\frac{L_{B,+}^2}{L_+^2} - 1\right), \tag{2}$$

where the free-positron lifetime in the perfect ZrO_2 lattice was taken as $\tau_B \approx 133$ ps on the basis of the theoretical calculations of Sec. III A, L_+ and $L_{B,+}$ denote the mean positron diffusion lengths measured on the single crystal and a perfect ZrO_2 lattice, respectively. The latter quantity for ZrO_2 is not known and was assumed to equal ≈150 nm, which is a typical mean positron diffusion length in similar materials.[61] The symbol ν denotes the specific positron trapping rate. Here we used $\nu \approx 10^{14}$ at. s^{-1}, which is a typical value for monovacancies in most solids.[38] The defect concentration estimated from Eq. (2) is then $C \approx 2$ at. %. Despite of uncertainties of input quantities, Eq. (2) implies a very high defect concentration comparable in order of magnitude with the concentration of yttrium atoms in the crystal (5.5 at. %). This testifies that the defects responsible for positron trapping in the ZrO_2+9 mol. % Y_2O_3 single crystal must be of a structural origin. Hence, LT studies strongly indicate that positrons in ZrO_2+9 mol. % Y_2O_3 single crystal are trapped at defects which contain V_{Zr}''''. However, the lifetime measured in experiment is shorter that the lifetime calculated for positrons trapped in V_{Zr}'''', see Table V. This shortening of positron lifetime may be caused by two factors: (i) inward relaxation of O anions due to attractive Coulomb interaction with positron trapped in vacancy (see Sec. III A) or (ii) formation of complexes of V_{Zr}'''' with certain impurities (e.g., hydrogen). Clearly, more investigations are needed to clarify this problem.

The DBP ratio curve measured on the ZrO_2+9 mol. % Y_2O_3 single crystal is plotted in Fig. 5 (open circles). The curve exhibits a distinct peak around a momentum of $p \approx 15 \times 10^{-3} m_0 c$, which is known to be characteristic of positron annihilations with oxygen in the lattice[62] and represents a contribution of positrons annihilating with $2p$ oxygen electrons. A rather high contribution of positrons annihilated by oxygen electrons is visible in the figure. It favors positron trapping in a defect the surrounding of which is similar to that of V_{Zr}'''', since Zr vacancies have eight NN oxygen atoms and a contribution coming from annihilations with oxygen electrons is, therefore, expected to dominate. It should be mentioned that a very similar ratio curve (including even the magnitude of the peak at $p \approx 15 \times 10^{-3} m_0 c$) was recently measured[9] in CDB experiments on a ZrO_2+9.5 mol. % Y_2O_3 single crystal of a different producer (Alfa Aesar, USA).

As discussed above in this section, all positrons in the ZrO_2+9 mol. % Y_2O_3 single crystal annihilate from a single state, i.e., trapped in a single type of defect. Hence, the DBP is a superposition of partial profiles, n_{Zr}, n_O, and n_Y arising from the annihilation of trapped positrons with zirconium, oxygen, and yttrium electrons, respectively,

$$n = x_{Zr} n_{Zr} + x_O n_O + x_Y n_Y. \tag{3}$$

Here x_{Zr}, x_O, and x_Y denote the fractions of positrons annihilated by zirconium, oxygen, and yttrium electrons, respectively, in the given type of defects.

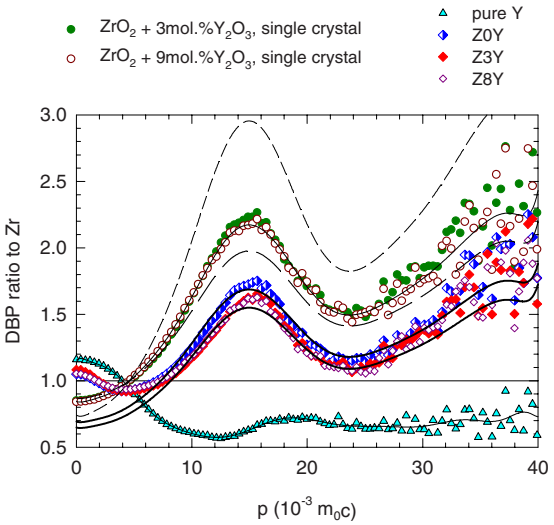

FIG. 5. (Color online) The measured DBP ratio curves for YSZ single crystals and pressure-compacted binary YSZ nanopowders (P=500 MPa). The DBP ratio curve for a well-annealed pure Y sample is plotted in the figure as well. The DBP ratio curves determined from Eq. (4) of Sec. III B for a hypothetical case, when all positrons annihilate with oxygen electrons only, and for the perfect ZrO_2 single crystal are plotted by the thin short- and long-dashed lines, respectively. The thick solid lines show approximations of DBP ratios for the pure ZrO_2 and an YSZ compacted nanopowders given by Eq. (14) of Sec. III C. Thin solid lines are polynomial smoothing curves plotted just to guide an eye.

Let us first consider the contribution of Y electrons. The DBP ratio curve measured on the well-annealed pure yttrium, see triangles in Fig. 5, exhibits a broad minimum at $p \approx 13 \times 10^{-3} m_0 c$ and becomes rather flat at $p > 18 \times 10^{-3} m_0 c$ due to a similar electronic structure of yttrium and zirconium. It is known that yttrium is coupled with $V_O^{\bullet\bullet}$ (Ref. 9), but theoretical calculations in Sec. III A showed that neither the $Y'_{Zr}V_O^{\bullet\bullet}Y'_{Zr}$ nor the $2Y'_{Zr}V_O^{\bullet\bullet}Zr_{Zr}^{\times}V_O^{\bullet\bullet}2Y'_{Zr}$ complexes may be considered as effective positrons traps. The only defect identified in Sec. III A as a potential trapping center for positrons is V_{Zr}''''. As there is no indication of yttrium coupling with V_{Zr}'''', the fraction of positrons annihilated by Y electrons in the ZrO_2+9 mol. % Y_2O_3 should be very small and can be neglected to a first approximation.

This argumentation is further supported by the present CDB observations, see Fig. 5, which are showing no traces of yttrium contribution to the total DBP ratio for the ZrO_2 +9 mol. % Y_2O_3 single crystal. To be certain about this conclusion, we measured also a DBP for the ZrO_2+3 mol. % Y_2O_3 single crystal (empty circles shown on Fig. 5). Despite of three times lower concentration of Y_2O_3, the DBP ratio observed for the ZrO_2+3 mol. % Y_2O_3 single crystal is almost identical with that for ZrO_2+9 mol. % Y_2O_3. Hence, a reasonable approximation of the DBP ratio curve for these YSZ single crystals is

$$\rho = \frac{n}{n_{Zr}} \approx 1 - x_O + x_O \rho_O, \tag{4}$$

where $\rho_O \equiv n_O / n_{Zr}$ is the ratio curve for positrons annihilated by oxygen electrons, i.e., for a hypothetical situation where

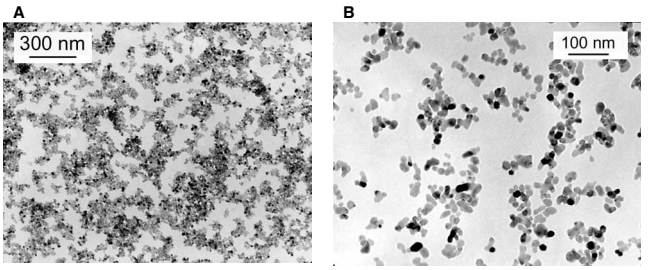

FIG. 6. TEM images (two different magnifications) of calcinated nanopowders of ZrO_2+3 mol. % Y_2O_3 prior to compaction.

all positrons annihilate *exclusively* with oxygen electrons. In theoretical calculations (Sec. III A) it was found that the fraction of positrons annihilated by oxygen is $x_O \approx 0.7$ for positrons trapped at V_{Zr}''''. Thus, assuming that positrons in a ZrO_2+9 mol. % Y_2O_3 single crystal are trapped at defects similar to V_{Zr}'''', we can calculate the DBP ratio ρ_O from Eq. (4). This curve representing the "pure" contribution arising from annihilations of positrons with oxygen electrons is plotted in Fig. 5 by a short-dashed line.

On the other hand, for a free positron delocalized in a perfect ZrO_2 lattice the expected probabilities of annihilation with oxygen or zirconium electrons are almost the same, i.e., $x_O \approx 0.5$, see Sec. III A. The DBP ratio curve expected for a delocalized positron in a perfect ZrO_2 lattice can be, therefore, easily calculated from ρ_O and is also plotted in Fig. 5 by a long-dashed line. It has to be mentioned that the n_O curve for a positron in a perfect ZrO_2 may differ slightly from that for a positron trapped in V_{Zr}''''-like defects. However, these curves differ mainly in the low-momentum range where the contribution from valence electrons dominates. Localized core electron orbitals, however, are not involved in crystal bonds and remain, therefore, basically unaffected by the atomic environment. As far as the high-momentum part is considered, the shape of both curves is similar.

C. Nanocrystalline powders

YSZ nanopowders

XRD and TEM characterizations. The structure of YSZ nanopowders was directly observed by TEM and XRD. In Fig. 6, TEM images of the calcinated ZrO_2+3 mol. % Y_2O_3 nanopowders (prior to compaction) are shown as an example. The mean particle size of the YSZ nanopowders is determined from broadening of XRD lines by using the Scherer formula and fell within (23 ± 2), (18 ± 1), and (16 ± 1) nm for ZrO_2 with 0, 3, and 8 mol. % of Y_2O_3 stabilizer content, respectively. These values agree well with the particle sizes estimated from TEM observations.

The XRD spectrum of ZrO_2+3 mol. % Y_2O_3 compacted nanopowder (compaction pressure $P=500$ MPa) is presented in Fig. 7. The specimen exhibits a tetragonal phase pattern with lattice parameters $a=5.121(2)$ Å and $c=5.131(2)$ Å. The c/a ratio for the compacted nanopowder is smaller than that reported for a tetragonal phase polycrystal,[63] but is comparable to that measured on YSZ nanopowders produced by a sol-gel method.[64] It should be mentioned, however, that tetragonal and cubic phases have very similar lattice parameters which makes it difficult to distinguish between them. The tetragonal structure can be identified only from a characteristic splitting of the Bragg profiles from the "c" index planes. However, due to a very small particle size, these split peaks of the tetragonal phase overlap with each other. Therefore, one cannot exclude to have a mixture of tetragonal and cubic phase in the compacted nanopowders.

One can see in Fig. 7 too that not only the position but also the intensity of the reflections measured on the compacted nanopowder agree well with the calculated pattern for the tetragonal ZrO_2 phase.[63] This testifies that grains in the compacted nanopowder are randomly oriented. The grain size (i.e., the size of coherently scattering domains) determined from integral breath of diffraction profiles using the Scherer formula is (17.0 ± 0.9) nm and corresponds well with the mean particle size determined prior to compaction. This demonstrates that the size of crystallites was not changed during compaction of nanopowders.

LT spectra. LT spectra of compacted nanocrystalline YSZ powders were decomposed into four exponential components (except for the para-Ps and the source contributions). Lifetimes, τ_i, and relative intensities, I_i, of these components for YSZ specimens with various Y_2O_3 content and compaction pressure, P, are collected in Table VI. It is clear from the lifetimes of the table and from the preceding discussion of results on single crystals in Sec. III B that all positrons in the compacted nanopowders annihilate either from trapped states at defects (saturated trapping) or form Ps. One can see from the table that the compacted nanopowders exhibit similar LT results independently of applied pressure. Obviously, the LT parameters for compacted binary YSZ nanopowders investigated in the present work do not vary significantly with the applied pressure in the 250–1000 MPa interval.

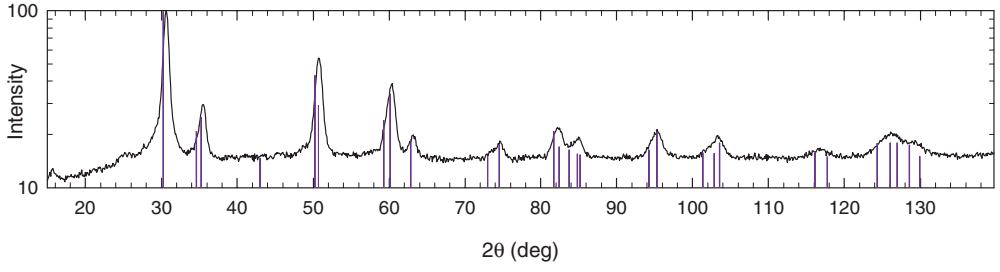

FIG. 7. (Color online) XRD spectrum of Z3Y compacted nanopowder ($P=500$ MPa). The calculated reflections for the tetragonal phase (Ref. 63) are plotted as vertical lines.

TABLE VI. LT results for the pressure-compacted binary YSZ nanopowders with various content of Y_2O_3 (lifetimes τ_i, relative intensities I_i, $i=1,\ldots,4$). Standard deviations are given in parentheses in units of the last significant digit. In addition to the components shown in the table, a p-Ps contribution with the fixed lifetime at 0.125 ns and relative intensity of $(I_3+I_4)/3$ was assumed in all decompositions. Intensities are normalized so that $I_1+I_2+4(I_3+I_4)/3=100$.

Material	P (MPa)	τ_1 (ns)	I_1 (%)	τ_2 (ns)	I_2 (%)	τ_3 (ns)	I_3 (%)	τ_4 (ns)	I_4 (%)
ZrO_2	250	0.185(2)	43(2)	0.370(4)	46(2)	1.9(1)	1.8(1)	31(2)	6.3(3)
	500	0.187(3)	42(2)	0.377(4)	48(2)	1.8(1)	1.5(1)	31(2)	5.7(3)
	1000	0.193(2)	44(2)	0.374(4)	44(2)	2.0(1)	2.3(1)	31(2)	6.0(3)
Z3Y	250	0.181(2)	33(2)	0.381(3)	58(2)	2.0(2)	1.2(1)	31(2)	5.4(3)
	500	0.174(3)	27(2)	0.373(3)	63(2)	1.6(1)	1.4(1)	30(2)	5.9(3)
	1000	0.180(4)	25(2)	0.369(3)	63(2)	1.7(1)	2.0(1)	28(2)	7.1(3)
Z8Y	250	0.187(3)	30(2)	0.375(4)	60(3)	2.0(2)	1.2(1)	30(2)	5.5(3)
	500	0.185(3)	30(2)	0.365(4)	60(2)	2.2(1)	2.1(1)	26(2)	5.0(3)
	1000	0.197(3)	31(2)	0.378(3)	58(2)	2.2(2)	1.6(1)	31(2)	5.9(3)

There are, however, remarkable differences between specimens with various Y_2O_3 content. On the one hand, the observed positron lifetimes are almost independent of the Y_2O_3 concentration testifying that the open volume related to defects and hence the nature of defects remain unchanged. The lifetime $\tau_1 \sim 185$ ps can be attributed to vacancylike defects. The second component with lifetime $\tau_2 \sim 375$ ps comes from larger defects with open volume comparable to a few monovacancies. On the other hand, the intensity ratios of the two shorter components, I_2/I_1, vary remarkably with the content of Y_2O_3 stabilizer. A more detailed treatment of this behavior will be given in the next paragraph.

In the lifetime region above 1 ns, the two components arising from annihilation of o-Ps could be resolved. In all cases, the total contribution of Ps annihilation to LT spectra remains below 10%. The principal o-Ps component ($\tau_4 \approx 30$ ns, $I_4 \approx 6\%$) corresponds to mesopores of ~ 3 nm diameter estimated on the basis of the semiempirical correlation between the o-Ps pick-off lifetime and the cavity size.[65] Compacted nanopowders usually contain some residual porosity.[66–68] Hence, the principal o-Ps component can be attributed to o-Ps localized in big cavities between crystallites. It was shown that cavities of such a size may appear between primary particles of ≈ 20 nm diameter.[7] The shorter and weaker o-Ps component with lifetime $\tau_3 \sim 2$ ns can be attributed to smaller voids with diameter ~ 0.6 nm estimated using the Tao-Eldrup model.[66,69] These sub-nanometer voids may be situated at intersections of crystallite interfaces. However, one cannot exclude another possibility that size distribution of cavities between grains is rather broad and the shorter o-Ps component is an artifact of the mesopore-size distribution tail extended to smaller pore sizes.

Relation of I_2/I_1 to grain size. The nanocrystalline structure leads to a significant volume fraction occupied by GB's. Due to a very small grain size (much smaller than typical mean positron diffusion lengths in a variety of defect-free materials[61]), positrons thermalized inside grains are expected to reach easily GB's during their lifetime. It is known that GB's in compacted nanocrystalline powders have a strongly disordered structure with a high density of open-volume defects.[70] Hence, one can expect that positrons become trapped and annihilate in these open-volume defects at GB's. It is also known that GB's in an ionic crystal may carry an electric potential resulting from the presence of the excess ions of one sign.[71] This potential is compensated by a space-charge layer of the opposite sign adjacent to GB's.

The electrical potential of GB's in YSZ's was intensively studied by Guo in Refs. 72 and 73. It was found that GB interfaces in YSZ are positively charged due to segregation of yttrium, which was clearly observed in experiment.[74–76] The positively charged GB interfaces in YSZ are, therefore, very likely surrounded by the negatively charged compensating layers characterized by depletion of $V_O^{\bullet\bullet}$ (Ref. 73). It is believed[72] that these space-charge layers with $V_O^{\bullet\bullet}$ depletion along GB's are responsible for a high electrical resistivity of GB's.

Thus, taking into account the above considerations and despite of yet unclear points, the most probable interpretation of the positron behavior in compacted YSZ nanopowders is that positrons which did not form Ps annihilate almost exclusively at GB's or inside the negatively charged layers associated to GB's from a trapped state at two kinds of defects: (i) vacancylike defects, which are the open-volume misfit defects present due to the disordered structure of GB's and (ii) larger point defects (vacancy clusters) with an open volume comparable to a few monovacancies situated in intersections of two or more GB's. In this respect, it should be mentioned that an amorphous phase was found by high-resolution TEM in intersection of GB's in YSZ sintered ceramics.[74] It should also be mentioned that, in general, positively charged regions, such as GB's in YSZ, repulse positrons, but as shown in Refs. 72 and 77, the size of the potential barrier is just a few tenths of eV, which does not prevent positrons from getting trapped in much deeper positron potential wells at the GB core.

The GB interface itself as well as the space-charge layer along a GB is an areal defect with two macroscopic dimensions. The volume density, C_L, of these structures is, therefore, proportional to the inverse of the grain size d. Assuming that vacancylike defects are uniformly distributed within

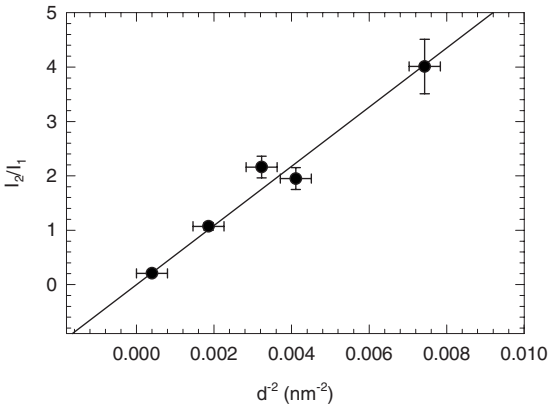

FIG. 8. Ratio I_2/I_1 against the inverse square of the particle size d for the compacted binary YSZ nanopowders with various Y_2O_3 content.

these layers with the areal density ξ_V, the volume concentration of the vacancylike defects, C_V, is

$$C_V = \xi_V C_L \sim \frac{1}{d}. \tag{5}$$

On the other hand, vacancy clusters at intersections of GB's are point defects. In the case of uniform grain size, there is a constant number of these vacancy clusters per grain. Thus, the volume concentration of vacancy clusters at intersections of GB's, C_t, is proportional to the number of grains in a unit volume, viz.,

$$C_t \sim \frac{1}{d^3}. \tag{6}$$

Due to saturated trapping at defects occurring in the studied compacted nanopowders, the ratio of relative intensities I_2 and I_1 equals to the ratio of positron trapping rates to corresponding defects,

$$\frac{I_2}{I_1} = \frac{\kappa_t}{\kappa_V} = \frac{\nu_t C_t}{\nu_V C_V}, \tag{7}$$

where κ_t and κ_V are positron trapping rates to vacancy clusters at intersections of GB's and vacancylike defects, respectively, and ν_t and ν_V are the corresponding positron-specific trapping rates. A combination of Eqs. (5)–(7) gives a simple relation between the ratio of relative intensities and the grain size

$$\frac{I_2}{I_1} \sim \frac{1}{d^2} \tag{8}$$

or

$$d = k\sqrt{\frac{I_1}{I_2}}. \tag{9}$$

The ratio I_2/I_1 is plotted in Fig. 8 for all the binary YSZ nanopowders studied versus d^{-2} determined by XRD. Because PAS results for YSZ specimens with the same Y_2O_3 content but compacted using various pressures are virtually the same, see Table VI, we plot in the figure the arithmetical average of I_2/I_1 ratios for these specimens to decrease the statistical scattering. In order to increase the range of grain sizes used to examine the correlation of I_2/I_1 ratio with grain size, two additional specimens are included in Fig. 8, namely, monoclinic ZrO_2 nanopowder with mean grain size of (50 ± 5) nm and cubic ZrO_2+3 mol. % Y_2O_3 with 0.3 mol. % of Cr_2O_3 stabilizer added in order to prevent particle clustering during calcination. For the latter sample the mean grain size determined by XRD is (12 ± 1) nm only. One can see in the figure that a dependence of I_2/I_1 on d^{-2} can indeed be considered as a linear relation testifying that our interpretation of the positron behavior in the compacted nanopowders is correct. From a linear fit of the Eq. (9) to the data in Fig. 8 one can derive the value of the proportionality constant $k=(24 \pm 4)$ nm.

The constant k in Eq. (9) depends on the areal density ξ_V of vacancylike defects in the grain surface layer and the ratio of the specific trapping rates for vacancylike defects and defects at intersections of GB's. Provided that this constant has been determined for a given class of materials, Eq. (9) can be used to estimate the mean grain size from LT results, which is certainly useful in many cases. Even if the constant k is not known, Eq. (9) can be still used to monitor relative changes in the grain size.

CDB results. The DBP ratios measured for the pure ZrO_2 nanopowder and two binary YSZ nanopowders with varying content of the Y_2O_3 stabilizer are plotted in Fig. 5 (P =500 MPa). Similarly to the single-crystal specimen, cf. Sec. III B, a distinct peak centered at $p \approx 15 \times 10^{-3} m_0 c$, which originates from positrons annihilated by oxygen electrons, appears in all these nanopowders. Compared to the single crystal, however, the magnitude of this peak is remarkably lowered. Another difference between the CDB results on compacted nanopowders and the single-crystalline specimen is an enhancement at very low momenta, which is clearly visible in Fig. 5 for the compacted nanopowders. This enhancement results from the p-Ps self-annihilation.

Contrary to Sec. III B, the total DBP, n, is to be expressed here as a superposition of contributions of *several* positron states existing in the specimen. On the basis of the present LT data, the following four positron states should be considered in compacted nanopowders: positrons trapped in (i) vacancylike defects and (ii) in vacancy clusters at the intersections of GB's, positrons that formed (iii) para- and (iv) ortho-Ps. Denoting corresponding partial DBP's as n_V, n_t, $n_{p\text{-}Ps}$, and $n_{o\text{-}Ps}$, respectively, we can write

$$n = (1 - f_t - f_{Ps})n_V + f_t n_t + \frac{1}{4} f_{Ps} n_{p\text{-}Ps} + \frac{3}{4} f_{Ps} n_{o\text{-}Ps}. \tag{10}$$

In this equation, f_t and f_{Ps}, respectively, are fractions of positrons annihilated as trapped in vacancy clusters at intersections of GB's and having formed Ps. The fraction of positrons annihilating from trapped state in vacancylike defects (presumably V''''_{Zr}-like defects, see Sec. III A) is then $f_V = 1 - f_t - f_{Ps}$. Fractions f_V, f_t, and f_{Ps} are given simply by corresponding relative intensities observed in the LT measurements (see Table VI),

$$100f_V = I_1, \quad 100f_t = I_2, \quad \text{and} \quad 100f_{Ps} = \frac{4}{3}(I_3 + I_4). \tag{11}$$

First, let's consider the pure ZrO_2 compacted nanopowder. In this case, positrons are annihilated by zirconium or oxygen electrons. In what follows, we will be interested in the high-momentum parts of DBP's, i.e., annihilations with high-momentum core electrons, which, contrary to the valence electrons, are only very slightly affected by crystal bonding and thus retain similar configuration as in the free atom orbitals. Therefore, one can assume that the shape of contributions n_{Zr} and n_O remains practically independent of the type of defect and partial DBP's can be in the high-momentum region expressed as

$$n_\alpha = x_{Zr}^\alpha n_{Zr} + x_O^\alpha n_O, \tag{12}$$

where superscript α=V, t, and o-Ps denotes a vacancylike defect, vacancy cluster at the intersection of GB's, or o-Ps, respectively. The symbols x_{Zr}^α and x_O^α, respectively, denote the relative fraction of positrons annihilated by zirconium and oxygen electrons, i.e., relative weight of these two elements and depends, therefore, on the local chemical environment of positron annihilation site. Because of p-Ps self-annihilation, $n_{p\text{-}Ps}$ can be fully neglected in the high-momentum region. Hence, the DBP for the pure ZrO_2 compacted nanopowder can be in the high-momentum region ($p > 10\times10^{-3}m_0c$) approximated as

$$n \approx (1 - f_t - f_{Ps})(x_{Zr}^V n_{Zr} + x_O^V n_O) + f_t(x_{Zr}^t n_{Zr} + x_O^t n_O) + \frac{3}{4}f_{Ps}(x_{Zr}^{o\text{-}Ps} n_{Zr} + x_O^{o\text{-}Ps} n_O). \tag{13}$$

The DBP ratio related to the pure Zr, $\rho = n/n_{Zr}$, is then given by expression

$$\rho \approx (1 - f_t - f_{Ps})(x_{Zr}^V + x_O^V \rho_O) + f_t(x_{Zr}^t + x_O^t \rho_O) + \frac{3}{4}f_{Ps}(x_{Zr}^{o\text{-}Ps} + x_O^{o\text{-}Ps} \rho_O). \tag{14}$$

Here ρ_O is the DBP ratio derived from the YSZ single-crystal data using Eq. (4) of Sec. III B (see also Fig. 5) for an idealized case when all positrons are annihilated by oxygen electrons.

The relative weights x_{Zr}^α and x_O^α can be estimated by theoretical calculations performed in Sec. III A. Hence, it is possible to model the DBP ratio curve by Eq. (14) using the fractions f_t and f_{Ps} obtained in LT measurement and relative weights x_{Zr}^α and x_O^α calculated for each considered defect. The ratio curve constructed using Eq. (14) can be then directly compared with experimental CDB ratio curve measured on pure ZrO_2 compacted nanopowder in order to test the validity of the interpretation of experimental LT spectrum, i.e., the assignment of resolved components to defects.

The following assumptions were used in modeling of the DBP curve: (i) the contribution of o-Ps pick-off annihilation to the total DBP is expected to resemble that of bulk ZrO_2 with approximately 1:1 ratio of positrons annihilated by oxygen and zirconium electrons, see Sec. III A, i.e., $x_O^{o\text{-}Ps} \approx x_{Zr}^{o\text{-}Ps} \approx 0.5$. (ii) Chemical surrounding of the vacancylike defects responsible for the LT component with lifetime τ_1 in Table VI was assumed to be closely similar to that of V_{Zr}''''. Theoretical calculations (Sec. III A) revealed that ≈70% of positrons trapped in zirconium vacancies is annihilated by oxygen electrons belonging mainly to the NN oxygen atoms. Hence we put $x_O^V = 0.7$ and $x_{Zr}^V = 0.3$. (iii) Theoretical calculations of positron parameters (within the ATSUP approach) were performed for a vacancy agglomerate consisting of four missing ZrO_2 units ($4V_{Zr}''''$'s and $8V_O^{\bullet\bullet}$'s) in order to model a vacancy cluster at the intersection of GB's and to estimate the x_O^t and x_{Zr}^t coefficients. These calculations revealed that positrons trapped at such vacancy agglomerates exhibit lifetime of ≈369 ps, which is comparable with the experimental lifetime τ_2 (see Table VI) and ≈30% of positrons trapped at vacancy aggregates are annihilated by oxygen electrons. Thus, for positrons trapped at vacancy clusters at the intersections of GB's we guess $x_O^t = 0.3$ and $x_{Zr}^t = 0.7$.

The ratio curve ρ for the pure ZrO_2 compacted nanopowder constructed using Eq. (14) is plotted in Fig. 5 by a thick solid line. Obviously, for high momenta $p > 8\times10^{-3}m_0c$, the curve determined by Eq. (14) is in very reasonable agreement with experimental data. We emphasize that no adjustable parameter was used in the modeling and the DBP curve ρ given by Eq. (14) is completely determined by the fractions f_t and f_{Ps} obtained independently from LT measurement and the assumptions (i)–(iii) made above in the preceding paragraph. As an alternative example, an assumption that the chemical surroundings of the vacancy clusters at the intersections of GB's is enriched with oxygen, i.e., it is similar to the environment of V_{Zr}'''', was examined. Such an assumption, however, lead to a ρ curve which is in a striking disagreement with experimental data.

In the case of compacted ZrO_2 nanopowder with the Y_2O_3 stabilizer, we do not expect that the yttrium contribution would be detectable in CDB experiments according to the discussion in Sec. III A 3. One can see in Fig. 5 that the DBP ratios for Z3Y and Z8Y compacted nanopowders are positioned below the curve for the pure ZrO_2 nanopowder. This shift occurs due to increased fraction of positrons trapped in vacancy clusters at intersections of GB's. This may be deduced from Table VI where I_2 intensities for stabilized powders are apparently larger (by about 15% on the expense of I_1) than that for the nonstabilized one. The DBP ratios for the YSZ compacted nanopowders were shown to be well approximated using the same assumptions as in the case of the pure ZrO_2 compacted nanopowder, assuming an enhanced fraction f_t reflecting enhanced intensity I_2 of positrons trapped in vacancy clusters at intersections of GB's (see the thick solid curve in Fig. 5).

The success of the DBP curves calculated using Eq. (14) to describe experimental points indicates that the assignment of LT components to defects given in this section is consistent with CDB results. From analysis of CDB curves we can draw the following conclusions. (i) The local chemical environment of vacancylike defects responsible for the shorter component with lifetime τ_1 in LT spectra, see Table VI, is very similar to that of Zr vacancy, i.e., positrons trapped at these defects are annihilated mainly by oxygen electrons. (ii) On the other hand, positrons trapped in the vacancy clusters

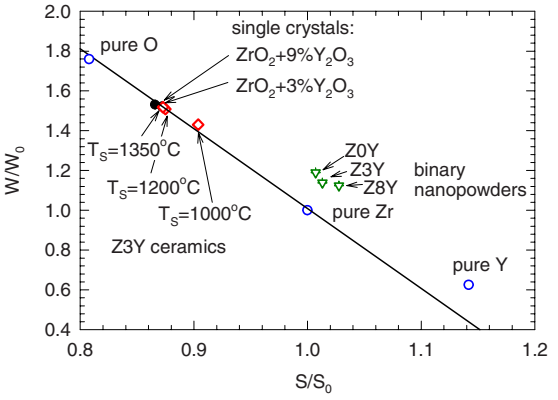

FIG. 9. (Color online) *S*-*W* plot constructed from CDB results. The *S* and *W* parameters are normalized to those for a well-annealed zirconium reference specimen. Open circles denote reference pure materials (the point for pure oxygen was calculated from the CDB profile n_O determined using Eq. (4) of Sec. III B. Full circles stand for YSZ single crystals, open triangles for binary YSZ compacted nanopowders (P=500 MPa), and open diamonds for ZrO_2 +3 mol. % Y_2O_3 sintered ceramics.

at intersections of GB's are annihilated predominantly by zirconium electrons. (iii) The decrease in magnitude of the "oxygen peak "located at $p \approx 15 \times 10^{-3} m_0 c$ in YSZ compacted nanopowders is caused by increased fraction f_t of positrons trapped in vacancy clusters at intersections of GB's due to decreasing grain size.

From the measured DBP's, the ordinary shape parameters, *S* and *W*, were calculated and arranged into the *S*-*W* plot in Fig. 9. All the *S* and *W* parameters were normalized to the values of S_{Zr}=0.501390(9) and W_{Zr}=0.10673(1), respectively, obtained for the well-annealed pure zirconium specimen. The *S*-*W* plot in Fig. 9 shows also the points for pure zirconium, pure oxygen (this point was obtained from $n_O = \rho_O n_{Zr}$), and pure yttrium. The points for compacted YSZ nanopowders are located aside the straight line connecting pure oxygen and pure zirconium points. This is due to the p-Ps contribution which significantly increases the *S* parameter.

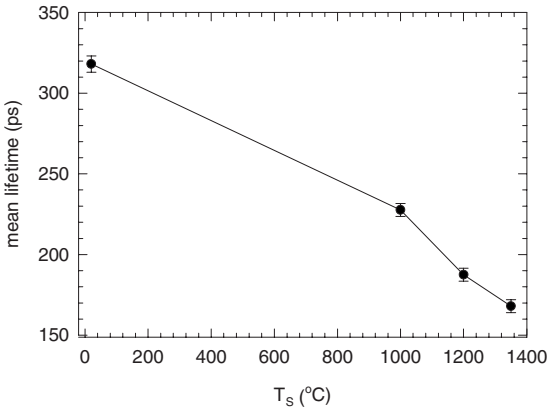

FIG. 10. ZrO_2+3 mol. % Y_2O_3 ceramics dependence of the mean positron lifetime on the sintering temperature T_S.

D. Sintered ceramics

LT results. ZrO_2+3 mol. % Y_2O_3 ceramics sintered at three different temperatures, T_S=1000, 1200, and 1350 °C, respectively, were investigated in the present work. Figure 10 shows the mean positron lifetime

$$\bar{\tau} = \sum_i \tau_i I_i \tag{15}$$

as a function of sintering temperature T_S. A substantial decrease in $\bar{\tau}$ with sintering temperature gives evidence for a recovery of open-volume defects during sintering.

It has to be mentioned that no Ps formation was observed in specimens subjected to sintering. Thus, the residual porosity (mesopores or voids) has been completely removed by sintering already at 1000 °C. This is in concordance with previous PAS investigations of sintered commercial ZrO_2 +2 mol. % Y_2O_3 nanopowders[10] which revealed that a disappearance of pores occurs in the range 800–1200 °C.

Two components with lifetimes $\tau_2 \approx 0.185$ and $\tau_3 \approx 0.380$ could be resolved in the samples sintered at T_S =1000 and 1200 °C. Development of lifetimes and relative intensities of the individual LT components with sintering temperature T_S is shown in Figs. 11(A) and 11(B), respec-

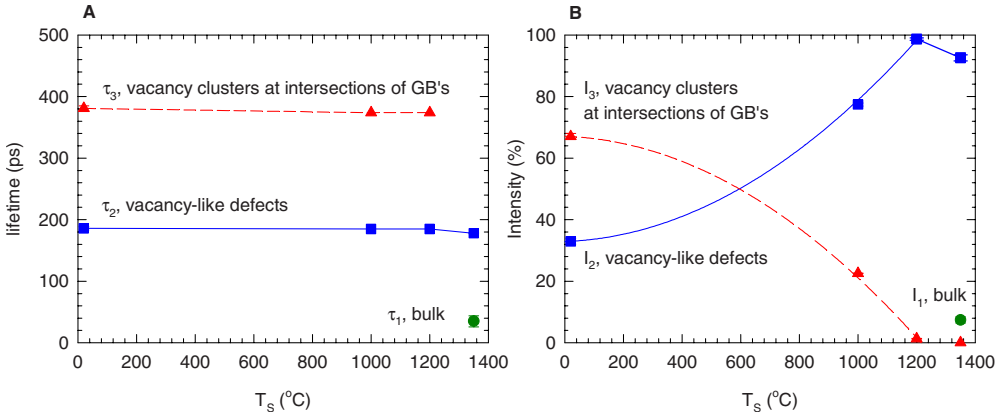

FIG. 11. (Color online) Individual LT components observed for ZrO_2+3 mol. % Y_2O_3 ceramics sintered at various temperatures: (a) positron lifetimes and (b) relative intensities.

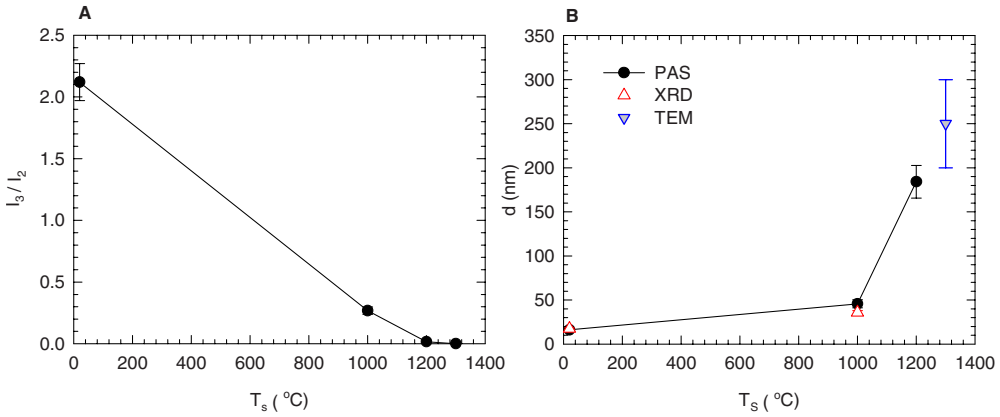

FIG. 12. (Color online) ZrO_2+3 mol. % Y_2O_3 ceramics sintered at various temperatures: (a) ratio I_3/I_2 and (b) mean grain size d calculated from PAS results using Eq. (9) as a function of the sintering temperature. Mean grain size estimated at selected sintering temperatures by XRD and TEM is also plotted in the figure for comparison.

tively. Obviously the lifetimes τ_2 and τ_3 of positrons trapped at defects do not change with sintering temperature. By analogy with compacted nanopowders, we attribute τ_2 and τ_3 components to positron trapping in vacancylike defects along GB's and in vacancy clusters at intersections of GB's, respectively. On the other hand, the intensity of positrons trapped in vacancy clusters at intersections of GB's, I_3, strongly decreases with increasing T_S due to grain growth in the specimens. The contribution of positrons trapped in vacancy clusters at intersections of GB's almost vanishes at $T_S=1200$ °C. A further increase in T_S to 1350 °C leads to the appearance of short-lived free-positron component with lifetime τ_1.

The ratio of intensities I_3/I_2 is plotted in Fig. 12(A) as a function of sintering temperature. A strong decrease in I_3/I_2 testifies that a significant grain growth takes place in the sintered ceramics. The mean grain size calculated from Eq. (9) is plotted in Fig. 12(B). The ceramic sintered at 1000 °C exhibits still a nanocrystalline grain size of $d\sim 50$ nm. But at higher sintering temperatures a pronounced grain growth occurs. A similar result was obtained in recent CDB investigations of ceramics sintered from a commercial nanopowder.[9]

The mean grain size determined in sintered ceramics by XRD and TEM is shown in Fig. 12(B) as well. One can see that there is fairly good agreement between the values determined from LT data and those obtained from XRD and TEM.

In the case of nanocrystalline specimens, the component with lifetime $\tau_2\sim 185$ ps comes *exclusively* from vacancylike defects situated at space-charge layers along GB's. However, when the grain size approaches the mean positron diffusion length, a contribution of positrons annihilated inside grain becomes important. In analogy with the YSZ single crystal, we expect that sintered ceramic contains a relatively high density of defects. If we assume that these defects are of the same kind as those in an YSZ single crystal, then they should contribute to LT spectrum by a component with lifetime of ≈ 175 ps, see Sec. III B. Because of closely spaced lifetimes, this component can hardly be distinguished from the components coming from the vacancylike defects in space-charge layers along GB's. Thus, the second component with lifetime τ_2 measured at the ceramic sintered at 1200 °C contains also an appreciable contribution from positrons trapped at vacancies inside grains. This causes a slight underestimation of grain size determined for this sintering temperature. At $T_S=1350$ °C positrons annihilate predominantly in the grain interiors and determination of grain size from LT results is not possible anymore.

Note that in the frame of the two-state simple trapping model[78] the quantity

$$\tau_f=\left(\frac{I_1}{\tau_1}+\frac{I_2}{\tau_2}\right)^{-1} \tag{16}$$

equals to the bulk positron lifetime in a defect-free material. For the ceramics sintered at $T_S=1350$ °C the Eq. (16) gives $\tau_f=(141\pm 5)$ ps, which is in a reasonable agreement with the calculated bulk lifetime in cubic ZrO_2, see Tables II and V.

CDB results. Figure 13 shows the DBP ratios for the ZrO_2+3 mol. % Y_2O_3 ceramics sintered at various temperatures. It is clear from the figure that the shape of these ratio curves for sintered ceramics differs remarkably from those measured on compacted nanopowders. With increasing sintering temperature the DBP ratios of sintered ceramic approach those for YSZ single crystals. This is clearly due to an increasing grain size and, thereby, diminishing of positron annihilation in the space-charge layers along GB's. A decrease in the curve at low momenta reflects a decreasing concentration of free volume defects (especially vacancy clusters at intersections of GB's) and also the fact that Ps is not formed in the sintered ceramics. The magnitude of the peak located at $p\approx 15\times 10^{-3}m_0c$ (annihilation with oxygen electrons) is raised with increasing T_S. This reflects the increasing fraction of positrons trapped in vacancylike defects inside grains on the detriment of positron trapping in vacancy clusters at intersections of GB's.

The DBP profile for YSZ ceramics sintered at $T_S<1350$ °C, i.e., at temperatures when no free positron component was detected in LT spectra can be expressed as

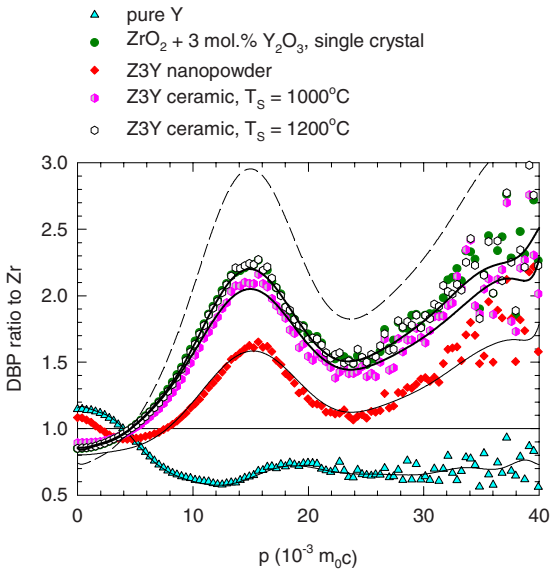

FIG. 13. (Color online) DBP ratios for ZrO_2+3 mol. % Y_2O_3 ceramics sintered at various temperatures T_S. The ratios for Z3Y compacted nanopowder and ZrO_2+3 mol. % Y_2O_3 single crystal are plotted in the figure as well. The reference DBP ratio for well-annealed pure yttrium is included in the figure. The DBP ratio determined from Eq. (4) for a hypothetical case when all positrons annihilate with oxygen electrons only is plotted by the thin dashed line. The thick solid lines show approximations of DBP ratios given by Eq. (18) for T_S=1000 and 1200 °C, respectively.

$$n = (1 - f_V - f_t)n_S + f_V n_V + f_t n_t, \tag{17}$$

where n_S represents DBP of positrons trapped at defects in the grain interiors. The contributions n_V and n_t are assumed to be the same as in YSZ compacted nanopowders, see Eq. (12). The DBP profile n_S can be expressed as

$$n_S = x_{Zr}^S n_{Zr} + x_O^S n_O + x_Y^S n_Y. \tag{18}$$

The contribution n_S arises from positron traps located in grain interiors, i.e., not in the yttrium enriched space-charge layer along GB's. Hence, x_Y^S is assumed to be very small ($x_Y^S \approx 0$). In order to obtain a good agreement with the experimental DBP ratio, it is necessary to assume that positrons trapped inside grains are annihilated predominantly by oxygen electrons ($x_O^S \approx 0.70$). This gives a hint that positrons inside grains are trapped in V_{Zr}''''.

One can see in the *S*-*W* plot (Fig. 9) that the data on sintered ceramics lie also on the line connecting the points for pure zirconium and oxygen. With increasing sintering temperature, the points move toward the single crystals, i.e., the fraction of positrons annihilated by oxygen electrons increases. This is due to grain growth, which reduces the contribution of positrons trapped in vacancy clusters at intersections of GB's.

IV. CONCLUSIONS

Various yttria-stabilized zirconia samples with different content of Y_2O_3 were investigated in the present work, i.e., single crystals, pressure-compacted nanopowders, and ceramics obtained by sintering the nanopowders. LT and CDB measurements with a conventional ^{22}Na positron source were carried out. In selected cases, they were supplemented with the SPIS technique. Comprehensive *ab initio* calculations of positron parameters were performed in order to assist the interpretation of experimental data. The obtained results are itemized below.

(1) Theoretical *ab-initio* calculations showed that neither positively charged $V_O^{\bullet\bullet}$ nor its neutral complexes with yttrium are capable of positron trapping at room temperature. On the other hand, V_{Zr}'''' is a deep positron trap.

(2) A ZrO_2+9 mol. % Y_2O_3 single crystal exhibits a high density of defects. Positrons trapped at these defects are predominantly annihilated by oxygen electrons. Taking into account positron lifetime and chemical surrounding, the most likely candidates for these defects are zirconium vacancies.

(3) Positrons in binary YSZ compacted nanopowders are trapped by vacancylike defects situated mainly in negative space-charge layers along grain boundaries or in vacancy clusters at intersections of GB's. Moreover, ~10% of positrons form Ps in large voids or pores.

(4) It was found that the ratio of relative intensities of positrons trapped in vacancy clusters at intersections of GB's and vacancylike defects is proportional to the inverse of square of grain size, $I_2/I_1 \sim d^{-2}$. This relation can be used for the determination of grain size from LT data. The mean grain size d determined by the LT method is in a good agreement with the ones obtained either by XRD or by TEM.

(5) Residual porosity in binary YSZ compacted nanopowders was removed by sintering at 1000 °C. Significant grain growth takes place during sintering at temperatures above 1000 °C.

ACKNOWLEDGMENTS

This work was granted by The Ministry of Schools, Youths and Sports of the Czech Republic under scientific Plan No. 0021620834 and project COST OC 165. Additional financial supports from The Academy of Science of The Czech Republic (Projects No. KAN300100801 and No. KJB101120906) and The National Academy of Science of Ukraine (Scientific Plans No. A 116/06 H and No. A 106U006933) are greatly appreciated.

*Corresponding author; jakub.cizek@mff.cuni.cz

[1] See, e.g., http://www.stanfordmaterials.com
[2] P. Hautojärvi and C. Corbel, in *Positron Spectroscopy of Solids*, edited by A. Dupasquier and A. P. Mills (IOS, Amsterdam, 1995), p. 609.
[3] J. R. MacDonald, K. G. Lynn, R. A. Boie, and M. F. Robins, Nucl. Instrum. Methods **153**, 189 (1978).
[4] R. Krause-Rehberg and H. S. Leipner, in *Positron Annihilation in Semiconductors: Defect Studies*, Springer Series in Solid-State Sciences Vol. 127, edited by M. Cardona, P. Fulde, K. von Klitzing, R. Merlin, H.-J. Queiser, and H. Störmer (Springer-Verlag, Berlin, 1999), p. 98.
[5] M. H. Weber and K. G. Lynn, in *Principles and Applications of Positron and Positronium Chemistry*, edited by Y. C. Yean, P. E. Mallon, and D. M. Schrader (World Scientific, Singapore, 2003), p. 167.
[6] M. J. Puska and R. M. Nieminen, J. Phys. F: Met. Phys. **13**, 333 (1983).
[7] K. Ito, Y. Yagi, S. Hirano, M. Miyayama, T. Kudo, A. Kishimoto, and Y. Ujihira, J. Ceram. Soc. Jpn. **107**, 123 (1999).
[8] Z. Wang, Z. W. Chen, J. Zhu, S. J. Wang, and X. Guo, Radiat. Phys. Chem. **58**, 697 (2000).
[9] J. E. Garay, S. C. Glade, P. Asoka-Kumar, U. Anselmi-Tamburini, and Z. A. Munir, J. Appl. Phys. **99**, 024313 (2006).
[10] Y. Yagi, S. Hirano, Y. Ujihira, and M. Miyayama, J. Mater. Sci. Lett. **18**, 205 (1999).
[11] J. Čížek, O. Melikhova, J. Kuriplach, I. Procházka, T. E. Konstantinova, and I. A. Danilenko, Phys. Status Solidi C **4**, 3847 (2007).
[12] O. Melikhova, J. Kuriplach, J. Čížek, I. Procházka, W. Anwand, G. Brauer, T. E. Konstantinova, and I. A. Danilenko, Phys. Status Solidi C **4**, 3831 (2007).
[13] I. Procházka, J. Čížek, J. Kuriplach, O. Melikhova, T. E. Konstantinova, and I. A. Danilenko, Acta Phys. Pol. A **113**, 1495 (2008).
[14] O. Melikhova, J. Kuriplach, J. Čížek, I. Procházka, and G. Brauer, Mater. Sci. Forum **607**, 125 (2009).
[15] J. Čížek, I. Procházka, O. Melikhova, J. Kuriplach, G. Grauer, W. Anwand, T. E. Konstantinova, and I. A. Danilenko, J. Phys.: Conf. Ser. (to be published).
[16] A. M. Korduban, I. A. Yashschishyn, T. E. Konstantinova, I. A. Danilenko, G. K. Volkova, and V. A. Glazunova, Adv. Funct. Mater. **14**, 454 (2007).
[17] T. Konstantinova, I. Danilenko, N. Pilipenko, and A. Dobrikov, *Ceramics: Getting into the 2000's: Part A* (Techna Group s.r.l., Faenza, Italy, 2004), p. 305.
[18] A. M. Slipenyuk, M. D. Glinchuk, I. P. Bykov, A. V. Ragulya, V. P. Klimenko, T. E. Konstantinova, and I. A. Danilenko, Ferroelectrics **298**, 289 (2004).
[19] E. Boroński and R. M. Nieminen, Phys. Rev. B **34**, 3820 (1986).
[20] B. Barbiellini, M. J. Puska, T. Torsti, and R. M. Nieminen, Phys. Rev. B **51**, 7341 (1995).
[21] F. Bečvář, J. Čížek, L. Lestak, I. Novotny, I. Procházka, and F. Sebesta, Nucl. Instrum. Methods Phys. Res. A **443**, 557 (2000).
[22] H. Surbeck, Helv. Phys. Acta **50**, 705 (1977).
[23] J. Čížek, F. Bečvář, I. Procházka, and J. Kočík, Mater. Sci. Forum **445-446**, 63 (2004).
[24] W. Anwand, H.-R. Kissener, and G. Brauer, Acta Phys. Pol. A **88**, 7 (1995).
[25] A. van Veen, H. Schut, M. Clement, J. de Nijs, A. Kruseman, and M. Ijpma, Appl. Surf. Sci. **85**, 216 (1995).
[26] F. A. Kröger, *Chemistry of Imperfect Crystals* (North-Holland, Amsterdam, 1974), Vol. 2.
[27] P. Li, I. Wei Chen, and J. E. Penner-Hahn, Phys. Rev. B **48**, 10063 (1993).
[28] B. W. Veal, A. G. McKale, A. P. Paulikas, S. J. Rothman, and L. J. Nowicki, Physica B **150**, 234 (1988).
[29] G. Stapper, M. Bernasconi, N. Nicoloso, and M. Parrinello, Phys. Rev. B **59**, 797 (1999).
[30] V. Butler, C. R. A. Catlow, and B. E. F. Fender, Solid State Ionics **5**, 539 (1981).
[31] E. C. Subbarao and H. S. Maiti, Solid State Ionics **11**, 317 (1984).
[32] J. P. Goff, W. Hayes, S. Hull, M. T. Hutchings, and K. N. Clausen, Phys. Rev. B **59**, 14202 (1999).
[33] M. Fèvre, A. Finel, and R. Caudron, Phys. Rev. B **72**, 104117 (2005).
[34] Z. R. Dai, Z. L. Wang, Y. R. Chen, H. Z. Wu, and W. X. Liu, Philos. Mag. A **73**, 415 (1996).
[35] R. J. D. Tilley, *Principles and Applications of Chemical Defects* (Stanley Thornes, Cheltenham, 1998).
[36] X. Guo, Solid State Ionics **99**, 137 (1997).
[37] A. S. Foster, V. B. Sulimov, F. Lopez Gejo, A. L. Shluger, and R. M. Nieminen, Phys. Rev. B **64**, 224108 (2001).
[38] M. J. Puska and R. M. Nieminen, Rev. Mod. Phys. **66**, 841 (1994).
[39] S. E. Kulkova, V. V. Kalchikhin, and O. N. Muryzhnikova, Solid State Commun. **84**, 497 (1992).
[40] A. P. Seitsonen, M. J. Puska, and R. M. Nieminen, Phys. Rev. B **51**, 14057 (1995).
[41] M. J. Puska, S. Mäkinen, M. Manninen, and R. M. Nieminen, Phys. Rev. B **39**, 7666 (1989).
[42] B. Kralik, E. K. Chang, and S. G. Louie, Phys. Rev. B **57**, 7027 (1998).
[43] X. Guo and Z. Wang, J. Eur. Ceram. Soc. **18**, 237 (1998).
[44] G. Brauer, W. Anwand, D. Grambole, J. Grenzer, W. Skorupa, J. Cizek, J. Kuriplach, I. Prochazka, C. C. Ling, C. K. So, D. Schulz, and D. Klimm, Phys. Rev. B **79**, 115212 (2009).
[45] G. Kresse and J. Hafner, Phys. Rev. B **47**, 558 (1993).
[46] G. Kresse and J. Hafner, Phys. Rev. B **49**, 14251 (1994).
[47] G. Kresse and J. Furthmüller, Comput. Mater. Sci. **6**, 15 (1996).
[48] G. Kresse and J. Furthmüller, Phys. Rev. B **54**, 11169 (1996).
[49] S. Ostanin, E. Salamatov, A. J. Craven, D. W. McComb, and D. Vlachos, Phys. Rev. B **66**, 132105 (2002).
[50] G. Kresse and D. Joubert, Phys. Rev. B **59**, 1758 (1999).
[51] G. Jomard, T. Petit, A. Pasturel, L. Magaud, G. Kresse, and J. Hafner, Phys. Rev. B **59**, 4044 (1999).
[52] L. Gilgien, G. Galli, F. Gygi, and R. Car, Phys. Rev. Lett. **72**, 3214 (1994).
[53] R. P. Feynman, Phys. Rev. **56**, 340 (1939).
[54] I. Makkonen, M. Hakala, and M. J. Puska, Phys. Rev. B **73**, 035103 (2006).
[55] J. Marley and R. Dockerty, Phys. Rev. **140**, A304 (1965).
[56] Y. Chen, V. M. Orera, R. Gonzalez, R. T. Williams, G. P. Williams, G. H. Rosenblatt, and G. J. Pogatshnik, Phys. Rev. B **42**, 1410 (1990).
[57] S. Hull, T. W. D. Farley, M. A. Hackett, W. Hayes, R. Osborn, N. H. Andersen, K. Clausen, M. T. Hutchings, and W. G. Stirling, Solid State Ionics **28**, 488 (1988).
[58] M. Alatalo, B. Barbiellini, M. Hakala, H. Kauppinen, T. Kor-

honen, M. J. Puska, K. Saarinen, P. Hautojärvi, and R. M. Nieminen, Phys. Rev. B **54**, 2397 (1996).
[59] J. Kuriplach, A. L. Morales, C. Dauwe, D. Segers, and M. Šob, Phys. Rev. B **58**, 10475 (1998).
[60] R. I. Grynszpan, S. Saude, L. Mazerolles, G. Brauer, and W. Anwand, Radiat. Phys. Chem. **76**, 333 (2007).
[61] T. E. M. Staab, R. Krause-Rehberg, and B. Kieback, J. Mater. Sci. **34**, 3833 (1999).
[62] U. Myler and P. J. Simpson, Phys. Rev. B **56**, 14303 (1997).
[63] D. N. Argyriou and C. J. Howard, J. Appl. Crystallogr. **28**, 206 (1995).
[64] R. Srinivasan, R. J. D. Angelis, G. Ice, and B. H. Davis, J. Mater. Res. **6**, 1287 (1991).
[65] K. Ito, H. Nakanishi, and Y. Ujihira, J. Phys. Chem. B **103**, 4555 (1999).
[66] M. Eldrup, D. Lightbody, and J. Sherwood, J. Chem. Phys. **63**, 51 (1981).
[67] R. Würschum, M. Scheytt, and H.-E. Schaefer, Phys. Status Solidi A **102**, 119 (1987).
[68] H.-E. Schaefer, R. Wurschum, R. Birringer, and H. Gleiter, Phys. Rev. B **38**, 9545 (1988).
[69] S. Tao, J. Chem. Phys. **56**, 5499 (1972).
[70] R. Birringer, Mater. Sci. Eng., A **117**, 33 (1989).
[71] W. D. Kingery, J. Am. Ceram. Soc. **57**, 1 (1974).
[72] X. Guo and R. Waser, Prog. Mater. Sci. **51**, 151 (2006).
[73] X. Guo, Solid State Ionics **81**, 235 (1995).
[74] S. Stemmer, J. Vleugels, and O. V. D. Biest, J. Eur. Ceram. Soc. **18**, 1565 (1998).
[75] A. J. A. Winnubst, P. J. M. Kroot, and A. J. Burggraaf, J. Phys. Chem. Solids **44**, 955 (1983).
[76] K. Matsui, H. Yoshida, and Y. Ikuhara, Acta Mater. **56**, 1315 (2008).
[77] X. Guo and Z. Zhang, Acta Mater. **51**, 2539 (2003).
[78] R. West, in *Positrons in Solids*, edited by P. Hautojärvi (Springer-Verlag, Berlin, 1979), p. 89.